



HAL
open science

Pearls on a String: Dark and Bright Galaxies on a Strikingly Straight and Narrow Filament

Maryam Arabsalmani, Sambit Roychowdhury, Benjamin Schneider, Volker Springel, Emeric Le Floc'H, Frederic Bournaud, Andreas Burkert, Jean-Charles Cuillandre, Pierre-Alain Duc, Eric Emsellem, et al.

► **To cite this version:**

Maryam Arabsalmani, Sambit Roychowdhury, Benjamin Schneider, Volker Springel, Emeric Le Floc'H, et al.. Pearls on a String: Dark and Bright Galaxies on a Strikingly Straight and Narrow Filament. The Astrophysical journal letters, 2025, 980 (1), pp.L2. 10.3847/2041-8213/ada779 . hal-04940022

HAL Id: hal-04940022

<https://hal.science/hal-04940022v1>

Submitted on 12 Feb 2025

HAL is a multi-disciplinary open access archive for the deposit and dissemination of scientific research documents, whether they are published or not. The documents may come from teaching and research institutions in France or abroad, or from public or private research centers.

L'archive ouverte pluridisciplinaire **HAL**, est destinée au dépôt et à la diffusion de documents scientifiques de niveau recherche, publiés ou non, émanant des établissements d'enseignement et de recherche français ou étrangers, des laboratoires publics ou privés.



Distributed under a Creative Commons Attribution 4.0 International License



Pearls on a String: Dark and Bright Galaxies on a Strikingly Straight and Narrow Filament

M. Arabsalmani^{1,2,14}, S. Roychowdhury^{2,3}, B. Schneider^{4,5}, V. Springel⁶, E. Le Floch⁷, F. Bournaud⁷, A. Burkert^{3,8}, J.-C. Cuillandre⁷, P.-A. Duc⁹, E. Emsellem^{10,11}, D. Galárraga-Espinosa⁶, E. Pian^{6,12}, F. Renaud^{9,13}, and M. A. Zwaan¹⁰

¹ Excellence Cluster ORIGINS, Boltzmannstraße 2, 85748 Garching, Germany; maryam.arabsalmani@origins-cluster.de

² Ludwig-Maximilians-Universität, Schellingstraße 4, 80799 München, Germany

³ University Observatory Munich (USM), Scheinerstraße 1, 81679 München, Germany

⁴ MIT Kavli Institute for Astrophysics and Space Research, 70 Vassar Street, Cambridge, MA 02139, USA

⁵ Aix Marseille University, CNRS, CNES, LAM, 58, bd Charles Livon -13284 Marseille Cedex, France

⁶ Max Planck Institute for Astrophysics, Karl-Schwarzschild-Straße 1, D-85748 Garching, Germany

⁷ Université Paris-Saclay, Université Paris Cité, CEA, CNRS, AIM, 91191, Gif-sur-Yvette, France

⁸ Max-Planck-Institut für extraterrestrische Physik (MPE), Giessenbachstr. 1, 85748 Garching, Germany

⁹ Université de Strasbourg, CNRS, Observatoire astronomique de Strasbourg, UMR 7550, F-67083 Strasbourg, France

¹⁰ European Southern Observatory, Karl-Schwarzschild-Straße 2, 85748 Garching, Germany

¹¹ Univ. Lyon, Univ. Lyon1, ENS de Lyon, CNRS, Centre de Recherche Astrophysique de Lyon, UMR5574, 69230 Saint-Genis-Laval, France

¹² INAF, Astrophysics and Space Science Observatory, via P. Gobetti 101, 40129 Bologna, Italy

¹³ University of Strasbourg Institute for Advanced Study, 5 allée du Général Rouvillois, F-67083 Strasbourg, France

Received 2024 September 14; revised 2024 December 23; accepted 2024 December 26; published 2025 February 5

Abstract

We identify a chain of galaxies along an almost straight line in the nearby Universe with a projected length of ~ 5 Mpc. The galaxies are distributed within projected distances of only 7–105 kpc from the axis of the identified filament. They have redshifts in a very small range of $z = 0.0361\text{--}0.0370$ so that their radial velocities are consistent with galaxy proper motions. The filament galaxies are mainly star forming and have stellar masses in a range of $10^{9.1}\text{--}10^{10.7} M_{\odot}$. We search for systems with similar geometrical properties in the full-sky mock galaxy catalog of the MillenniumTNG simulations and find that, although such straight filaments are unusual and rare, they are predicted by Λ CDM simulations (4% incidence). We study the cold H I gas in a 1.3 Mpc section of the filament through H I 21 cm emission line observations and detect 11 H I sources, many more than expected from the H I mass function in a similar volume. They have H I masses $10^{8.5}\text{--}10^{9.5} M_{\odot}$ and are mostly within ~ 120 kpc projected distance from the filament axis. None of these H I sources has a confirmed optical counterpart. Their darkness together with their large H I 21 cm line widths indicates that they contain gas that might not yet be virialized. These clouds must be marking the peaks of the dark matter and H I distributions over large scales within the filament. The presence of such gas clouds around the filament spines is predicted by simulations, but this is the first time that the existence of such clouds in a filament is observationally confirmed.

Unified Astronomy Thesaurus concepts: [Large-scale structure of the universe \(902\)](#); [Cosmic web \(330\)](#); [Dark matter distribution \(356\)](#); [Galaxy formation \(595\)](#); [Neutral hydrogen clouds \(1099\)](#)

1. Introduction

The dark and baryonic matter in the Universe is predicted to be distributed over an intriguing pattern, known as the cosmic web (Y. B. Zel'dovich 1970; J. R. Bond et al. 1996; V. Springel et al. 2005, 2006). This multiscale and highly interconnected network consists of knots, filaments, sheets, and voids, with dense knots at the intersection of filaments and filaments at the intersection of sheets. And these surround nearly empty void regions. The filaments, connecting massive galaxy clusters located at the knots, contain the largest fraction ($\sim 50\%$) of mass in the Universe (R. Cen & J. P. Ostriker 2006; M. A. Aragón-Calvo et al. 2010; M. Cautun et al. 2014). High-resolution simulations show that filaments are sparsely inhabited by halos and that galaxies make up only a few percent

of the baryonic mass in the filaments (M. Cautun et al. 2014; D. Martizzi et al. 2019). The dominating component of baryons in filaments is predicted to be the low-density, diffuse intergalactic medium and mainly at temperatures $10^5 \text{ K} \lesssim T \lesssim 10^7 \text{ K}$ (e.g., R. Cen & J. P. Ostriker 2006; D. Martizzi et al. 2019). The low densities of the filaments suggest that their identifications in observations are quite challenging.

Only a handful of intercluster filaments have been identified through the observations of X-ray emission or Sunyaev-Zel'dovich signal from the warm/hot phase between pairs of close clusters or inside superclusters in the nearby Universe (C. Scharf et al. 2000; D. Eckert et al. 2015; G. E. Alvarez et al. 2018; H. Tanimura et al. 2019, 2020b, 2020a). Such studies (mainly done through stacking) have succeeded in measuring the density and temperature of the densest parts of the warm/hot gas in the filaments around clusters. In terms of finding filaments, the primary approach, though, has been structure-finding algorithms based on the distribution of galaxies and galaxy clusters in large sky area databases (T. Sousbie et al. 2008; J. Jasche et al. 2010; E. Tempel et al. 2014; N. Malavasi et al. 2020; I. Santiago-Bautista et al. 2020), which has led to

¹⁴ Vera Rubin Fellow.

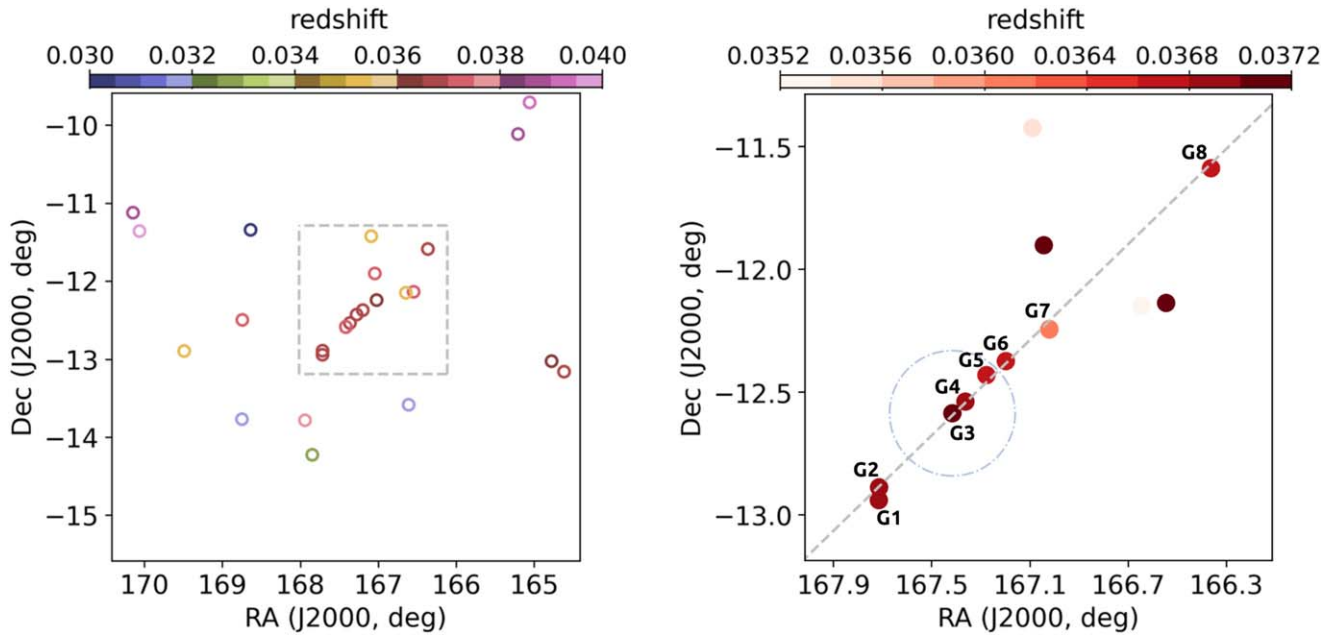


Figure 1. Left: $6^\circ \times 6^\circ$ image, centered at the position of 2MASX J11093966–1235116 (G3), showing galaxies with measured spectroscopic redshift listed in SIMBAD. We have also added LEDA 951348 (G4) with its redshift measured from the H I 21 cm emission line. The gray dashed box marks the frame of the right panel. Right: $2^\circ \times 2^\circ$ image, showing the eight galaxies (G1–G8) along the narrow filament (see Table 1 for galaxy properties). The gray dashed line shows the best-fit straight line to the positions of the eight galaxies. In both panels, the color of the points represents the redshift values of the galaxies following the representative color bars above the panels. The dotted–dashed blue circle (centered at the position of 2MASX J11093966–1235116, G3) marks the JVLA HPBW for the H I 21 cm emission line observations we present in this Letter.

the identification of a large number of filaments in the nearby Universe and their geometrical properties such as length and radius (see also S. Kim et al. 2016). In some cases, filaments have been identified through weak-lensing techniques (at $z \sim 0.5$; J. P. Dietrich et al. 2012; M. Jauzac et al. 2012; Y. Higuchi et al. 2015; N. Martinet et al. 2016; H. Kondo et al. 2020). At higher redshifts ($z > 2$), detection of rest-frame ultraviolet Ly α radiation through absorption has resulted in the identification of a few filaments (e.g., S. Cantalupo et al. 2014; D. C. Martin et al. 2015; H. Umehata et al. 2019; see also S. G. Gallego et al. 2018 for a stacking analysis). These studies have obtained indirect estimates of cold gas mass ($T \sim 10^4$ K) in the observed sections of the filaments and in some cases have found it to be significantly larger than what is predicted by simulations (e.g., S. Cantalupo et al. 2014).

Theoretical studies suggest that streaming of cold gas along the filaments plays a prominent role in the formation and growth of galaxies by providing the required gas for star formation (F. Bournaud et al. 2005; A. Dekel et al. 2009; M. Fumagalli et al. 2011). This gas component is not only expected to have very low densities, it is also predicted to comprise only a small fraction (a few percent) of the baryonic mass in the filaments (A. Popping et al. 2009; D. Martizzi et al. 2019; D. Galárraga-Espinosa et al. 2021). There have been attempts to detect the diffuse cold gas in the nearby filaments through H I 21 cm emission line observations (e.g., A. Popping & R. Braun 2011a, 2011b, 2011c), but none has been successful to date.

In this Letter, we report the identification of a strikingly narrow filament of galaxies in the nearby Universe. We chanced upon this filament while studying the environment of the galaxy 2MASX J11093966–1235116 (the host galaxy of gamma-ray burst, GRB, 171205A at $z = 0.037$; see M. Arabsalmani et al. 2022). We noticed the alignment of a number of H I sources that we had detected in the field of the

galaxy along a direction with a position angle of $\sim 45^\circ$ with respect to north. We then inspected the Pan-STARRS optical images of the field of the galaxy in large scales and found a number of galaxies aligned in the same direction, covering about 2° in the sky. The tantalizing possibility that these were marking a cosmic filament prompted us to further observe the field and investigate the properties of the identified galaxies and the H I sources, both in radio and optical wavelengths. The details of the observations used in this study are presented in Section 2. We describe and discuss our findings in Sections 3 and 4 and summarize them in Section 5. Throughout this Letter, we use a standard flat Λ CDM model with $H_0 = 69.6 \text{ km s}^{-1} \text{ Mpc}^{-1}$ and $\Omega_m = 0.286$.

2. Observations and Data Analysis

2.1. Karl J. Jansky Very Large Array Data and H I Source Identification

Observations with the L -band receivers of the Karl J. Jansky Very Large Array (JVLA) in the B and C configurations were used to map the H I 21 cm emission in a section of the identified filament. The observations in the B configuration, originally part of a program targeting the H I properties of the galaxy 2MASX J11093966–1235116, were carried out in 2019 March and 2019 May for a total time of ~ 10.5 hr (proposal ID: VLA/2018-07-058; PI: Arabsalmani). The JVLA primary beam was centered at the position of 2MASX J11093966–1235116. With a half-power primary beamwidth (HPBW) of $\sim 30'$ at the observed frequency in the L band, a 1.3 Mpc long section of the filament was covered within the HPBW (marked in the right panel of Figure 1).

Follow up C-configuration observations were carried out in 2022 October for a total time of ~ 17.5 hr (proposal ID: VLA/2022-00-109; PI: Arabsalmani) in order to study the same

Table 1
The Properties of the Eight Galaxies That Reside along a Narrow Filament Shown in the Right Panel of Figure 1

ID	Name as in Optical Surveys	R.A. (J2000)	Decl.(J2000)	Redshift ^a	$\log_{10}(M_*/M_\odot)$	$\log_{10}(\text{SFR}/M_\odot \text{ yr}^{-1})$	$E(B - V)$
G1	LEDA 114626	11:10:51.48	-12:56:27.3	0.03695 ± 0.00015	9.75 ± 0.03	-1.90 ± 0.07	0.1
G2	2MASX J11105122-1253193	11:10:51.22	-12:53:19.1	0.03697 ± 0.00015	10.70 ± 0.03	-1.70 ± 0.07	0.1
G3	2MASX J11093966-1235116	11:09:39.66	-12:35:11.6	0.03702 ± 0.00015	10.15 ± 0.03	0.10 ± 0.07	0.2
G4	LEDA 951348	11:09:26.97	-12:32:20.6	0.03691 ± 0.00012	9.10 ± 0.03	-0.80 ± 0.07	0
G5	LEDA 104056	11:09:06.43	-12:25:51.6	0.03673 ± 0.00022	9.80 ± 0.03	-0.70 ± 0.07	0.1
G6	2MASX J11084744-1222264	11:08:47.44	-12:22:26.6	0.03671 ± 0.00015	10.45 ± 0.03	0.10 ± 0.07	0.2
G7	2MASX J11080494-1214422	11:08:04.93	-12:14:42.2	0.03609 ± 0.00015	10.15 ± 0.08	-0.15 ± 0.18	0.2
G8	2MASX J11052703-1135216	11:05:27.05	-11:35:21.4	0.03674 ± 0.00015	10.20 ± 0.03	-1.30 ± 0.07	0

Notes. The last three columns list the stellar mass, SFR, and $E(B - V)$ of the galaxies obtained from the SED modeling (see Figure 8 for the best-fit SEDs). G1, G2, and G8, the three galaxies at the two ends of the filament, appear to be passive galaxies, while the remaining five galaxies are all actively making stars and are among the main-sequence galaxies.

^a The redshifts of G2, G3, G6, G7, and G8 are taken from the Final Release of 6dFGS (D. H. Jones et al. 2004, 2009). The redshifts of G1 and G5 are taken from the Las Campanas Redshift Survey (S. A. Shectman et al. 1996). For G4 (LEDA 951348), the redshift is obtained from the H I 21 cm emission line (M. Arabsalmani et al. 2022).

section of the identified filament. For both configurations, we used the JVLA software backend with 16 MHz bandwidth, centered on ~ 1.368 GHz, subdivided into 4096 channels, yielding a velocity resolution of ~ 0.9 km s⁻¹ and a total velocity coverage of ~ 3500 km s⁻¹. The bright calibrator 3C 286 and the secondary calibrator J1130-1449 were observed to calibrate the flux, the time-dependent part of the gain, and the system bandpass.

Following the procedure described in M. Arabsalmani et al. (2022), “Classic” AIPS (E. W. Greisen 2003) was used to calibrate, self-calibrate, subtract the continuum from the calibrated visibilities for each day’s data, and create cumulative visibility data sets separately for the B and C configurations (see Appendix A for more details). We also combined the residual visibilities from the full 5 days in order to create a combined B+C-configuration data set. The three sets of combined visibilities (B configuration, C configuration, and B+C configuration) were Fourier transformed to produce spectral cubes using the task IMAGR. For each configuration, we created two data cubes with optimized velocity resolutions of ~ 34 km s⁻¹ and ~ 50 km s⁻¹ to improve the statistical significance of the detected H I 21 cm emission in independent velocity channels while still having sufficient resolution to accurately trace the velocity field of any detected source. In order to optimize between the signal-to-noise ratio (SNR) of the detections and the spatial resolution, robust factors of 0.5, -0.5, and 0.5 were used for the B-configuration, C-configuration, and B+C-configuration visibilities, respectively, when creating the cubes, resulting in angular resolutions of $7''.5 \times 6''.4$, $20''.3 \times 17''.0$, and $10''.5 \times 9''.1$, respectively. The properties of the produced cubes are provided in Table 3 in Appendix A. We also applied the primary beam correction using the task PBCOR.

Identifications of H I sources were carried out in two steps. (i) We first did a blind search using the Source Finding Application (SoFiA) software (see Appendix A for more details). (ii) Next, for each of the sources identified by SoFiA, we created two separate spectra from the 35 and 50 km s⁻¹ data cubes. The spectra were extracted from the cubes in the regions defined based on the moment zero maps created by SoFiA. We only kept those detected H I sources that have SNRs of 5 and above in both the 35 and 50 km s⁻¹ cubes (see Figures 6 and 7 in Appendix A). We measured the H I integrated flux density by integrating over the adjacent channels with fluxes above the rms noise and converted this to a H I mass. We also fitted a

Gaussian function to the H I 21 cm emission line to measure the redshift and the FWHM of the emission.

2.2. CFHT Data and Optical Source Identification

We obtained deep multiband (u , g , r , and i) images of the same portion of the filament described in Section 2.1 with the MegaCam camera installed on the CFHT on 2022 April 16 (proposal ID: 22ad91; PI: Le Floch). As described in P.-A. Duc et al. (2015), the images were obtained by (a) consecutively acquiring seven individual images with large offsets between them, (b) building a master sky by median-stacking the individual images, and (c) subtracting a smoothed and rescaled version of the master sky from each individual image before stacking them. The final stacked images consist of 4×7 frames with a total exposure time of 82 minutes for the u band, 42 minutes for the g and r bands, and 27 minutes for the i band. The observations were obtained with an average seeing of $1''.1$ under photometric conditions. Images were processed by the low-surface-brightness branch of Elixir (Elixir-LSB). We estimate the upper limits of 29.5, 29.5, 29, and 28 mag arcsec⁻² for the local surface brightnesses in the u , g , r , and i bands, respectively.

To detect the possible optical counterparts of the H I sources, we ran the SExtractor software (E. Bertin & S. Arnouts 1996) in “double image” mode, using the deepest CFHT r -band image as the detection reference for all bands. This mode also ensures that object magnitudes were measured consistently for all images (e.g., aperture positions and sizes). We used the SExtractor MAG_AUTO parameter to measure the total flux of the detected sources in each image. To ensure detection of very faint optical sources, the detection threshold of SExtractor was set to 1σ , and spurious sources were removed manually after a visual inspection. In case of nondetection in a band, the image depth obtained with small blank apertures around the source position was used as an upper limit.

2.3. Ancillary Data

We used the SIMBAD astronomical database for creating a list of galaxies identified in optical surveys in the field around 2MASX J11093966-1235116. For the eight galaxies listed in Table 1, we used all the publicly available photometries (based on measurements of total fluxes) from the Two Micron All Sky Survey (2MASS), Galaxy Evolution Explorer (GALEX),

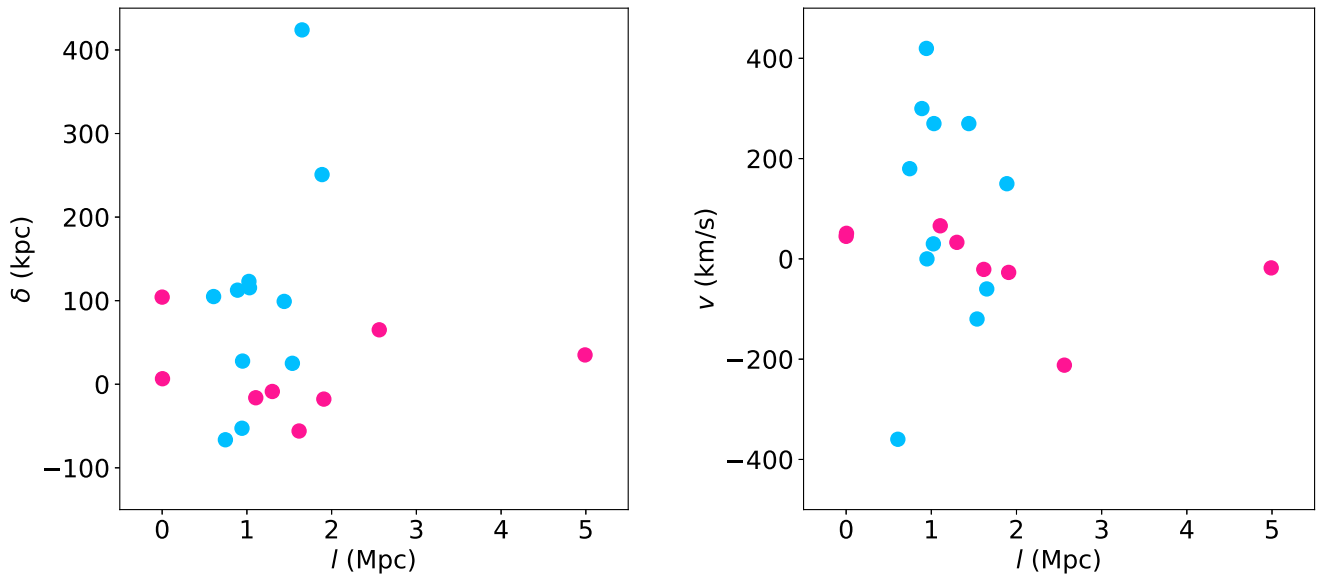


Figure 2. Left: the perpendicular (on-sky) distance to the filament axis, δ , vs. the distance along the filament axis from a reference point on the line, l . We have chosen G1 as the reference point, which is located at $l = 0$ (hence, G8 is located at $l = 4.99$ Mpc, the length of the filament). The filament axis is presented with the dashed line in the right panel of Figure 1. Right: the radial velocity with respect to $z_{\text{med}} = 0.0368$ (the median, and also the average, redshift of the eight galaxies on the filament), v , vs. l . The pink and blue points represent the eight galaxies and the 11 H I sources, respectively, in both panels.

Pan-STARRS, and Wide-field Infrared Survey Explorer (WISE). For the detected optical source candidates in our CFHT images, we used the publicly available photometries from the Legacy and WISE surveys (A. Dey et al. 2019). We cross-matched the magnitudes obtained from the CFHT images with those of the Legacy survey and found them to be consistent.

3. Results

3.1. A Narrow Filament of Galaxies

The left panel of Figure 1 shows the distribution of galaxies with known spectroscopic redshifts within a $6^\circ \times 6^\circ$ image, centered on the galaxy 2MASX J11093966–1235116 at $z = 0.037$. One can immediately distinguish the assembly of eight galaxies (hereafter G1–G8) along an almost straight line at $z \sim 0.037$. The right panel of the figure shows the eight galaxies G1–G8 lined up, creating a very straight galaxy chain. The redshifts of all galaxies but G4 are measured from optical spectroscopic data and are taken from S. A. Shectman et al. (1996) and D. H. Jones et al. (2004, 2009). For G4 (LEDA 951348), the redshift is derived from our H I 21 cm emission line observations (M. Arabsalmani et al. 2022). All the redshift measurements are quite accurate (see Table 1). These are in a very small range between $z = 0.03609$ and $z = 0.03702$, with a median redshift of $z_{\text{med}} = 0.03683$, same as the average redshift.

In order to investigate the structure of the galaxy chain in the perpendicular direction to the sky, we use the redshift measurements of G1–G8 and obtain their relative radial velocities with respect to $z_{\text{med}} = 0.0368$. These velocities, presented in the right panel of Figure 2, vary from -212 to 66 km s^{-1} , similar to the velocities expected from the proper motion of galaxies. This implies that G1–G8 are creating a very straight filament on the plane of the sky. One cannot fully discount the possibility that the slight differences in the redshifts of G1–G8 are due to their different distances (and not their proper motions); i.e., G1–G8 are distributed over a 2D

plane (sheet) rather than being along a filament on the plane of the sky. Investigating this possibility requires independent distance measurements to the galaxies, which are exceedingly difficult, if possible at all, given the distance to the sources and their properties and magnitudes (see, e.g., I. Steer et al. 2017). But the even distribution of the radial velocities of G1–G8 with respect to z_{med} (right panel of Figure 2) indicates that they are likely on the plane of the sky and hence belong to a filament.

Even more striking is the narrowness of the alignment on the plane of the sky. We fit a straight line to the positions of G1–G8 on the sky. This is shown with the dashed line in the right panel of Figure 1. The eight galaxies reside very close to this line (hereafter filament axis), with projected (on the sky) distances varying in a small range between 7 and 104 kpc. This is very small compared to the projected length of the filament, which is about 5 Mpc. The left panel of Figure 2 shows the distribution of the separation from the filament axis, δ , versus the distance along the line, l , both projected on the sky. We have chosen this reference point to be the projected position of G1 on the line, so that l is 0 and 4.99 Mpc for G1 and G8, respectively.

In principle, a chance alignment of galaxies in the plane of the sky can result in the filament we have identified. We cannot precisely determine the probability of such a chance alignment given that the identification of the filament was serendipitous and emerged while studying the field of a nearby GRB (a single field). However, the probability should be insignificant since the discovery was not based on a systematic search. Future studies are planned in order to address the probability of detecting such aligned systems by examining large data sets.

We note that there are several more objects, identified as galaxies in large surveys, whose on-sky locations are coincident with the filament. But these galaxies do not have spectroscopic redshift measurements (possibly for being too faint); hence, their association with the filament is not clear. We do not include these galaxies in this study, but further spectroscopic observations are planned for these objects in order to explore their association with the filament.

Table 2
The Detected H I Sources Marked in Figure 3 and Their Properties Obtained from Their H I 21 Cm Emission Lines

ID	$z_{\text{H I}}$	$\Delta v_{0.037}$ (km s^{-1})	$\text{FWHM}_{\text{H I}}$ (km s^{-1})	$\int SdV$ (mJy km s^{-1})	$\log_{10}(M_{\text{H I}}/M_{\odot})$	$M_{\text{H I}}/M_{*}$	$N(\text{H I})$ (cm^{-2})	SNR_{35}	SNR_{50}	Array
(1)	(2)	(3)	(4)	(5)	(6)	(7)	(8)	(9)	(10)	(11)
G3	0.0370	3	317 ± 58	501 ± 47	9.50 ± 0.04	0.2	6.1×10^{20}	11	10	B
G4	0.0369	-27	117 ± 18	485 ± 53	9.49 ± 0.05	2.5	6.2×10^{20}	9	9	B
G5	0.0367	-92	170 ± 37	83 ± 14	8.72 ± 0.07	0.1	2.8×10^{20}	6	5	B+C
$(M_{\text{H I}}/M_{*})_{\text{LL}}$										
S1	0.0356	-428	127 ± 34	198 ± 37	9.10 ± 0.08	89	2.8×10^{20}	5	5	B+C
S2 ^a	0.0341	-875	132 ± 45	139 ± 29	8.95 ± 0.08	1	2.7×10^{20}	6	5	B+C
S3	0.0378	245	209 ± 59	102 ± 20	8.81 ± 0.08	2570	6.6×10^{20}	5	6	B
S4	0.0369	-21	112 ± 26	156 ± 25	9.00 ± 0.07	10,000	5.9×10^{20}	6	6	B
S5	0.0377	199	177 ± 56	133 ± 24	8.93 ± 0.07	$13/5370^{\text{b}}$	6.7×10^{20}	6	5	B
S6	0.0374	108	178 ± 45	198 ± 35	9.10 ± 0.08	1000	6.4×10^{20}	6	7	B
S7	0.0368	-46	229 ± 58	50 ± 9	8.50 ± 0.07	316	1.6×10^{20}	6	5	B+C
S8	0.0382	369	304 ± 105	45 ± 9	8.46 ± 0.09	912	2.1×10^{20}	5	7	B+C
S9	0.0377	216	126 ± 33	110 ± 18	8.85 ± 0.07	224	1.8×10^{20}	6	5	B+C
S10	0.0373	83	424 ± 91	386 ± 60	9.39 ± 0.06	15,488	8.1×10^{20}	6	5	B
S11	0.0364	-190	134 ± 29	199 ± 36	9.10 ± 0.08	96	7.8×10^{20}	6	6	B
S12	0.0366	-124	203 ± 42	203 ± 31	9.11 ± 0.06	28	9.3×10^{19}	7	7	C

Notes. Columns (2)–(6) are, respectively, redshift obtained from the H I 21 cm emission line, velocity offset of the H I 21 cm emission with respect to $z = 0.037$, FWHM of the H I 21 cm emission line, integrated flux density of the H I 21 cm emission line, and H I mass. Column (7) is the ratio of the H I mass to stellar mass for G3–G5 and the lower limit on $M_{\text{H I}}/M_{*}$ for the rest of the H I sources assuming that all the optical sources listed in Table 5 in Appendix B are associated with the H I sources. Column (8) is the H I column density equivalent to the 3σ level of emission in a single channel with a velocity width of 34 km s^{-1} (see Figure 5 in Appendix A for the H I contours). Columns (9)–(11) are the SNRs of the H I 21 cm emission line detected in cubes with channel widths of 35 and 50 km s^{-1} and the array configuration used for detecting the H I source and obtaining the H I spectrum.

^a The H I spectrum of this source is affected by systematics of unknown origin (see Section 3.2 for details). We therefore exclude this source from our analysis.

^b For this source, we have provided the $M_{\text{H I}}/M_{*}$ ratio including/excluding the optical source that is outside the H I emission (marked by “e” in Figure 5 in Appendix A).

We model the spectral energy distribution (SED) of G1–G8 using LePhare (S. Arnouts et al. 1999; O. Ilbert et al. 2006) through GAZPAR (galaxy redshifts and physical parameters) community service in order to obtain their stellar properties, such as stellar mass and star formation rate (SFR) values. These properties are listed in Table 1 (the fitted SEDs are provided in Appendix B). The galaxy stellar masses are in a range of $10^{9.1} - 10^{10.7} M_{\odot}$. G1, G2, and G8, the three galaxies at the two ends of the filament, appear to be passive galaxies based on their location on the M_{*} –SFR plane (J. Brinchmann et al. 2004). The color–color diagram analysis (S. Arnouts et al. 2013) confirms that G2 is indeed a passive galaxy but suggests that G8 is transiting from star forming to passive. The limited photometries for G1 do not allow studying its position in the color–color diagram. The remaining five galaxies all lie within the star-forming main-sequence galaxies on the M_{*} –SFR plane and are also categorized as star-forming galaxies based on the galaxy color–color diagram. Using the H I 21 cm emission line observations in the 1.3 Mpc long section of the filament (see Section 2.1), we measure the H I masses for G3, G4, and G5, listed in Table 2. We find G3 and G4 to be gas-rich galaxies with H I masses above average for their stellar masses (see B. Catinella et al. 2018 for the M_{*} – $M_{\text{H I}}$ relation of nearby galaxies). The $M_{\text{H I}}/M_{*}$ ratio of G5, though, is toward the lower side of the M_{*} – $M_{\text{H I}}$ relation.

3.2. Dark H I Clouds on the Filament

The HPBW of JVLA in our H I 21 cm emission line observations, marked with a dotted–dashed blue circle in the right panel of Figure 1, covers a 1.3 Mpc long portion of the

filament centered at G3. We restrict mapping the H I 21 cm emission line to within the JVLA HPBW in order to only detect H I emission with high sensitivity. We identify 15 H I sources in this region, all marked on the r -band CFHT image presented in Figure 3. The H I properties of these sources, including the (spectroscopic) redshift measurements obtained from their H I 21 cm emission lines, are listed in Table 2. The H I masses are within a range of $10^{8.5} - 10^{9.5} M_{*}$, and the H I 21 cm line widths vary in a range of $110 - 420 \text{ km s}^{-1}$.

Three of the detected sources are associated with G3, G4, and G5. Note that we do not detect the H I 21 cm emission line for G6 as expected, since this galaxy falls out of the JVLA HPBW. One of the detected H I sources, S2, is spatially coincident with a spiral galaxy with no measured spectroscopic redshift in optical surveys. This galaxy resides at a projected distance of 12 kpc from the filament axis (the dashed line in the right panel of Figure 1). We obtain a redshift of $z = 0.0341$ from the H I 21 cm emission line of this source, consistent with the photometric redshift of $z < 0.2$ that we obtain from modeling the SED of the galaxy. However, we detect signatures of systematics, appearing like absorption features over a velocity width of $\sim 1000 \text{ km s}^{-1}$ in the H I 21 cm spectrum of this source (see Figures 6 and 7 in Appendix A). We examine these features in the intensity map of the source and find them not to be present. In addition, no continuum emission in our JVLA observations is detected at the location of S2. We therefore conclude that the apparent features in the spectrum are due to systematics of unknown origin. This could have affected the redshift measured from the H I 21 cm

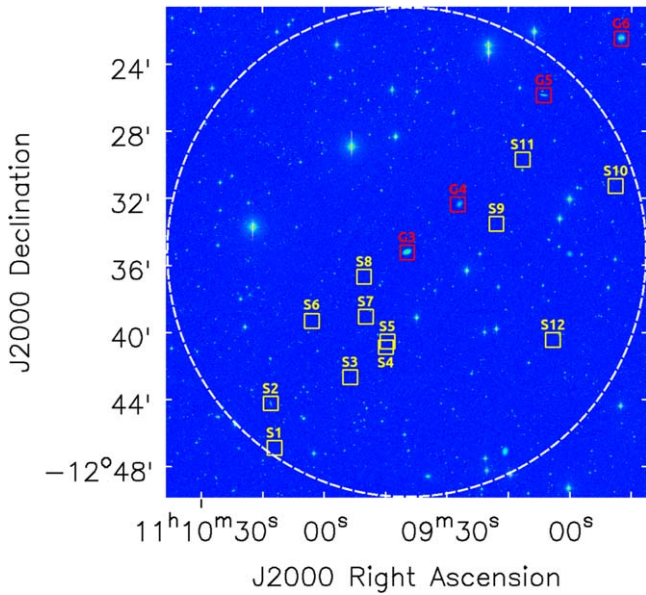


Figure 3. The r -band CFHT image, with the squares marking the positions of the HI sources detected within the JVLA HPBW (listed in Table 2). G3–G6 are marked with red squares. The HPBW of JVLA is marked with a white dashed circle.

emission of this source. We therefore exclude this source from any further analysis.

The remaining 11 sources are distributed along the filament, with projected distances of 25–424 kpc from the filament axis. They are marked with blue circles in Figure 2. Nine out of the 11 HI sources are located within 123 kpc from the filament axis, similar to the δ range for G1–G8. Only two sources, S10 and S12, are located at slightly larger distances of $\delta = 251$ and 424 kpc, respectively. We also derive the radial velocities of these sources with respect to $z_{\text{med}} = 0.0368$. These are within a range between -360 and 420 km s^{-1} and are shown in the right panel of Figure 2. The radial velocities of the HI sources are somewhat larger than those of G1–G8.

We search for the optical counterparts of the 11 HI sources using our deep, multiband CFHT images (see Section 2.2 for the magnitude limits). For each HI source, we identify all the detected optical sources within the extent of the HI emission. This extent is defined by the 1σ contour of the total HI emission. For each of the identified optical sources, we model the SED with LePhare (through GAZPAR) and obtain the probability distribution of the photometric redshift (z_{phot}) based on modeling its SED. Most of the identified optical sources are very unlikely to have $z_{\text{phot}} \lesssim 0.1$ (with probabilities of $< 1\%$; see Appendix B for more details).

To very conservatively estimate the lower limit of M_{HI}/M_* for each HI source, we assume that those optical counterpart candidates with a $\gtrsim 1\%$ probability of having $z_{\text{phot}} \lesssim 0.1$ are associated with the HI cloud. These are marked with yellow circles in the middle panel of Figure 5 in Appendix A. Assuming a redshift of $z = 0.0368$ (the median/average redshift of G1–G8) for these sources, we model their SEDs and estimate their stellar masses. By adding the stellar masses of the associated optical sources for each HI cloud, we obtain the corresponding M_{HI}/M_* for the HI cloud. The estimated M_{HI}/M_* values are listed in Table 2. These are within a range of ~ 30 – $15,500$, with a median of ~ 900 . Note that the actual HI masses for our detected HI sources should be larger than

what we have estimated given that the performed JVLA observations are not sensitive to low column densities ($N(\text{HI}) \leq$ a few times 10^{20} cm^{-2} , depending on the array configuration), making the M_{HI}/M_* estimates even more conservative. This implies that the HI sources that we have detected in the filament are quite dim/dark.

4. Discussion

4.1. The Peculiarity of the Filament

Following the identification of large numbers of filaments in the nearby Universe, mainly through structure-finding algorithms, the geometrical properties of the filaments have been studied in detail. Filament lengths are reported to vary from a few Mpc up to ~ 150 Mpc, with typical lengths of a few tens of Mpc (e.g., E. Tempel et al. 2014; V. Bonjean et al. 2020; I. Santiago-Bautista et al. 2020). The radii of the nearby filaments are found to be around or more than 1 Mpc, consistent with predictions from simulations (e.g., M. Cautun et al. 2014). Filament galaxies are typically at distances > 100 kpc from the filament spine (see, e.g., V. Bonjean et al. 2020; I. Santiago-Bautista et al. 2020; G. Castignani et al. 2022), with typical distances of about a few Mpc in most cases. In contrast, the filament we present here has all its identified galaxies residing at distances of $\lesssim 100$ kpc (mainly a few tens of kiloparsecs) from its axis, making this system strikingly narrow (see the left panel of Figure 2). With a ~ 5 Mpc length, this filament is among the shortest filaments that have been identified. D. Galárraga-Espinosa et al. (2020) examined the geometrical properties of the simulated filaments in TNG simulations and found that short filaments with lengths of a few Mpc are puffier than long filaments. Therefore, the short length of the presented filament here makes its narrowness even more unusual. In addition to its narrowness, the straightness of this filament is quite intriguing.

Although the low number of galaxies (eight) in the narrow filament does not allow a statistical comparison with the properties of large filament galaxy samples, we find that the properties of the eight galaxies stand out. Properties of filament galaxies have been extensively studied in order to explore the effect of filaments (predicted by simulations) on the formation and evolution of galaxies (M. Alpaslan et al. 2016; H. J. Martínez et al. 2016; D. Kleiner et al. 2017; T. Kuutma et al. 2017; N. Malavasi et al. 2017; K. Kraljic et al. 2018; C. Laigle et al. 2018; F. Sarron et al. 2019; V. Bonjean et al. 2020; G. Castignani et al. 2022; C. T. Donnan et al. 2022). The focus of these investigations has been on how the properties of galaxies change as one moves toward the spines of the filaments. Most of these studies find an increase in the fraction of passive galaxies compared to star-forming galaxies when going closer to filament spines. At fixed stellar mass, C. Laigle et al. (2018) showed that passive galaxies are found closer to their filament than active star-forming galaxies. N. Malavasi et al. (2017) reported the presence of the most massive and quiescent galaxies closer to the filament axis. G. Castignani et al. (2022) found the number of quenched galaxies at close distances to filaments to be significantly larger than that of active galaxies. Keeping in mind the low number of galaxies, it is notable that five out of the eight galaxies in this filament are actively forming stars. This is particularly interesting given that the eight galaxies are very close to the filament axis (7–104 kpc). In all the studies mentioned above, the filament

galaxies are typically at distances >100 kpc from the filament spine; i.e., the star-forming galaxies are at much larger distances from the filament spines compared to what we find here.

It is notable that the star-forming galaxies in the filament are within its midsection, quite away from the two nodes. These star-forming galaxies are predicted to fall into the nodes of the filament where passive galaxies reside. The concentration of the star-forming galaxies in the middle of the filament might indicate that the filament is in its initial evolutionary stages.

In order to assess the rarity of the identified narrow filament based on theoretical predictions, we use the filament catalog of the TNG300-1 simulations at $z = 0$ (D. Galárraga-Espinosa et al. 2020) to search for filaments with similar galaxy and geometrical properties in the TNG catalogs. This catalog is built up using the discrete persistent structure extractor (DisPerSe) algorithm (T. Sousbie 2011), which operates in 3D and detects filaments based on the galaxy density field. At first, we select filaments with lengths within a range of 4–6 Mpc containing seven to nine galaxies of stellar masses $10^{9.1} - 10^{10.7} M_{\odot}$ within 100 kpc from the filament spine. We do not put any constraint on the number of galaxies that the filaments might contain at distances larger than 100 kpc from their spines. We also allow selecting filaments that contain any number of galaxies with stellar masses $<10^{9.1} M_{\odot}$ or $>10^{10.7} M_{\odot}$ within 100 kpc from their spines. With these constraints, we find only 13 filaments out of 10,106 filaments in the filament catalog, but more importantly, none is like the filament we have identified.

None of the selected 13 filaments is nearly as straight, and all of them are much thicker, with a few tens of galaxies at distances of 100 kpc to 1 Mpc from the spine. Several (>10) of these galaxies have stellar masses of $10^{10} - 10^{12} M_{\odot}$ —well above the detection limit of large galaxy surveys in the field of the identified filament. The environment of the filament we present here is much emptier. There are only three galaxies detected in large galaxy surveys (with $\gtrsim 10^{10} M_{\odot}$) within the 1 Mpc distance of the filament axis (see Figure 1). Two of them (2MASX J11081033–1154122 and 2MASX J11061093–1208193), at distances of 630 and 740 kpc from the filament axis, are at $z \sim 0.037$, the redshift of the filament, and the third galaxy (2MASX J11063472–1209059) is at $z \sim 0.035$ (~ 500 km s^{-1} with respect to $z_{\text{med}} = 0.0368$). We also note that in 11 out of the 13 selected filaments, all the filament galaxies are passive, and in the remaining two filaments only one or two of the filament galaxies are star-forming.

The narrow and straight filament we have identified seems to have no match in the TNG catalog mentioned above. This, however, could be a result of how the catalog has been built up, i.e., using the DisPerSe method. For instance, in 10 out of the 13 selected filaments in the catalog, all the filament galaxies are located in a ~ 0.5 Mpc long section along the filament. This, perhaps, is expected given that the DisPerSe algorithm works based on identifying the peaks of the galaxy density.

In order to further investigate whether the existence of the filament we have identified challenges Λ CDM and our understanding of structure formation, we perform a more comprehensive comparison with the simulations. To do so, we make use of the full-sky mock galaxy catalog computed by M. Barrera et al. (2023) as part of the MillenniumTNG simulation project (C. Hernández-Aguayo et al. 2023), using a 740 Mpc box with 4320^3 simulation particles. The galaxy

catalog is produced in a completely seamless fashion for the backward light cone of a fiducial observer. We first select all galaxies in the redshift interval $0.0360 < z < 0.0371$ and with stellar mass $10^9 M_{\odot} < M_{\star} < 10^{11} M_{\odot}$, closely matching the characteristics of our filament galaxies. We then construct a set of 12,288 observational fields of 2° on a side based on pointings that uniformly cover the sky with the help of a Healpix tessellation of the unit sphere. To account for the centering onto the filament we carry out in our observational analysis, we first identify all galaxies in a spherical aperture with a radius of 2° around each of our pointings and then adopt the center of mass of the identified galaxies as the new center. We then constrain to the galaxies in a circular region of radius $\sqrt{2}^{\circ}$ around the new center and compute a second-order shape tensor for the 2D distribution of galaxies, allowing us to determine the major and minor axes. We also turn the galaxy distribution such that the major axis lies approximately diagonal and then restrict to a $2^{\circ} \times 2^{\circ}$ square-shaped field, just like in our observations shown in the right panel of Figure 1. We only keep fields that have between 8 and 12 galaxies in them, in order to closely mock up the conditions we have in our observational field. This leaves 1017 fields in our sample.

Finally, for the galaxies in each remaining field, we compute the average distance $\langle D \rangle$ of the galaxies to the major axis—which we identify as the filament spine—and the maximum extension of the galaxies along the filament direction, L_{max} . We then use these two quantities to define a dimensionless “thinness” quantity $T = \langle D \rangle / L_{\text{max}}$ that measures how narrow the galaxy distribution is. We can also measure the value of T for our observed filament, i.e., the eight galaxies G1–G8 plus the two galaxies that have somewhat larger distances from this filament spine. This yields $T_{\text{obs}} = 0.035$.

In the top two and bottom left panels of Figure 4, we show three examples of filamentary galaxy distributions found in this way, all with T values lower than T_{obs} . They indeed look comparably straight and narrow. In the bottom right panel of Figure 4, we examine this quantitatively in terms of the distribution of T over all 1017 of our fields. The vertical dashed red line marks the observed galaxy distribution. The observations are in the tail of the distribution, confirming that the filament is indeed unusual and rare. But it is not exceptionally uncommon. About 4% of our fields have comparable or even smaller values for the thinness parameter, so some fairly straight filaments can be found and are expected in the Λ CDM galaxy distribution as well.

4.2. Dark Clouds: Peaks of Dark Matter and HI Distributions

In addition to the peculiarity of the filament in its geometrical properties, the identification of several dark HI clouds in the filament is quite intriguing. The number of HI sources we have detected in the field exceeds the average number of HI sources that is typically detected in a similar volume. In order to estimate the excess of the HI source count, we use the local HI mass function derived for large HI surveys. We calculate the average number of HI sources (i) within the HI mass range of $10^{8.5} - 10^{9.5} M_{\odot}$, the mass range of our detected HI sources, and (ii) in a volume corresponding to a cylinder with a base as large as the HPBW of JVLA (marked with a white dashed circle in Figure 3) and a perpendicular distance of $d_l(z = 0.0382) - d_l(z = 0.0356)$. Here, $d_l(z)$ is the luminosity distance at redshift z , and $z = 0.0382$ and $z = 0.0356$ are the maximum and minimum redshifts of our detected HI sources, respectively. Using the HI mass function

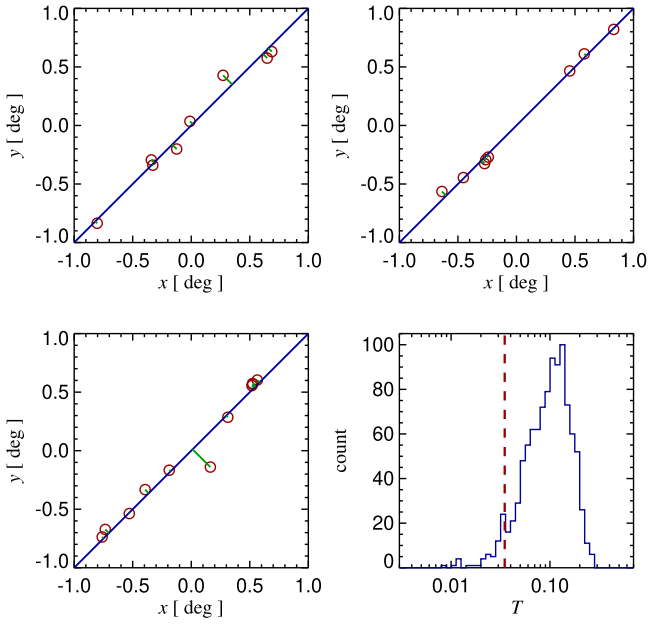


Figure 4. Three examples for $2^\circ \times 2^\circ$ fields in the full-sky galaxy light cone of the MillenniumTNG simulation, selected to contain galaxies with similar masses and redshifts as observed and to exhibit a similarly long and narrow filamentary distribution. We measure the thinness of the galaxy distribution through a quantity T defined as the ratio between the averaged perpendicular distances (green) between galaxies and the ridgeline of their filament (blue) and the length of the extension of the galaxy distribution in the filament direction. The histogram in the bottom right panel shows the distribution of this quantity for the 1017 fields we have with matching galaxy number density. For our observed galaxy distribution, the value of the thinness parameter is $T_{\text{obs}} = 0.035$ (vertical dashed line). About 4% of the fields have an equal or lower value for T , implying that the configuration we have discovered is rare in Λ CDM, but not exceptionally so.

of the HIPASS survey presented in M. A. Zwaan et al. (2005; see their Figure 1 and their best-fit parameters for a Schechter function), we find the average number of HI sources to be 0.16 ± 0.04 . This is even lower (0.11 ± 0.01) when we use the HI mass function of the ALFALFA survey presented in M. G. Jones et al. (2018; see their Figure 2 and their best-fit parameters for a Schechter function). The number of HI sources that we have detected (see Table 2 and Figure 3) is about 100 times larger than that expected from the average counts in large HI surveys.

The HI clouds we have detected in the filament have larger radial velocities compared to the eight galaxies in the filament (see the right panel of Figure 2). This might imply that they are at larger distances (in 3D) from the filament axis and hence in regions with lower densities. On the other hand, the galaxies (that have formed stars) are in higher-density regions close to the filament axis. We also note that the typical distances between the HI sources (the 11 HI clouds and the three galaxies with detected HI presented in Figure 3) are ~ 180 kpc. We do not have sufficient information to infer a robust origin (e.g., environment, filament characteristics, Jeans scale length, etc.) for this preferred length scale.

Previous studies of HI in filaments resulted in the identification of only one HI source with no known optical counterpart (in DSS images) among 199 detected sources (A. Popping & R. Braun 2011c). The reported source was detected at $N(\text{HI}) \sim 10^{19} \text{ cm}^{-2}$, with a narrow line width of about 20 km s^{-1} . The dark HI clouds that we identify in the filament are all detected at $N(\text{HI}) \geq \text{a few times } 10^{20} \text{ cm}^{-2}$,

with HI line widths $> 100 \text{ km s}^{-1}$. Their HI masses are in the range $10^{8.5} - 10^{9.5} M_\odot$, and their M_{HI}/M_* lower limits are within a range of $\sim 30 - 15,500$, with a median of ~ 900 . Nearby galaxies with $M_* \gtrsim 10^8 M_\odot$ typically have $M_{\text{HI}}/M_* \lesssim 10$ (see H. Dénes et al. 2014; B. Catinella et al. 2018 for HIPASS and xGASS surveys). Galaxies with lower stellar masses, though, are found to have higher HI mass fractions. In particular, low surface brightness and irregular galaxies are shown to have M_{HI}/M_* as high as 100 (see, e.g., L. Leisman et al. 2017; S. Mahajan et al. 2018).

The extremely large HI mass fractions that we obtain for the HI clouds are comparable with, and in some cases exceed, the highest HI mass fraction ever reported for dark systems, even those in galaxy groups and clusters. Several studies have reported $M_{\text{HI}}/M_* < 100$ for dark galaxy candidates (e.g., J. M. Cannon et al. 2015; S. Janowiecki et al. 2015; M. Bilek et al. 2020; J. Román et al. 2021). L. Leisman et al. (2021) measured $M_{\text{HI}}/M_* \sim 100$ for an extended HI cloud with $M_{\text{HI}} = 10^{9.3} M_\odot$. Even a threshold of $M_{\text{HI}}/M_* > 200$ defines 8 out of the 11 HI clouds we have detected in the filament as dark. This only decreases to six systems with a threshold of $M_{\text{HI}}/M_* > 900$. Such large HI mass ratios for dark clouds have only been reported in dense environments such as galaxy groups and clusters. G. I. G. Józsa et al. (2022) detected a massive chain of seven HI clouds in a galaxy group and found $M/M_* \sim 1200$, still smaller than the HI mass fractions that we measure for half of the HI clouds in the narrow filament. K. Lee-Waddell et al. (2014) reported the presence of a HI cloud with $M_{\text{HI}} = 10^{9.3} M_\odot$ and $M_{\text{HI}}/M_* \sim 2000$ (although with a velocity width of only a few tens of kilometers per second) in a galaxy group (see also O. I. Wong et al. 2021 for dark clouds in galaxy groups; and B. R. Kent et al. 2007; B. R. Kent 2010; A. Sorgho et al. 2017 for dark clouds in the Virgo cluster). Very recently, M. G. Jones et al. (2024) identified an extremely gas-rich, low-mass, star-forming galaxy in the Virgo cluster formed via extreme ram pressure stripping events with an extreme HI mass fraction of $\sim 20,000$. All these studies argue that the detected dark HI clouds within galaxy groups/clusters are the remnants of interacting systems or tidal features that survive in high-density environments.

Although our HI 21 cm line observations are not sensitive enough to detect the diffuse HI gas, the dark HI clouds we have detected must resemble the peaks of the large-scale HI distribution in the filament. Such HI peaks are in fact predicted by simulations to exist around the filament spines at high redshifts (e.g., see Figure 1 of Y. S. Lu et al. 2024 for high-resolution simulations of filaments at $z \sim 4$). These massive gas clouds, with no stars, are expected to reside in the dark matter halos along the filaments. Most of the HI clouds we detect in the filament have large HI 21 cm line widths for their masses. This together with their darkness could indicate that they belong to halos that recently made it to the cold core of the filament and contain gas that might not yet have virialized, thus not forming stars, as predicted for high-redshift filaments (e.g., Y. S. Lu et al. 2024). Note, though, that the HI clouds we detect should also contain gas in the “cold neutral phase” with temperatures of $\lesssim 600 \text{ K}$ given their high HI column densities ($N(\text{HI}) \geq \text{a few times } 10^{20} \text{ cm}^{-2}$; N. Kanekar et al. 2011). We emphasize that the properties of the filament we have identified in the local Universe can in principle be very different from those at high redshifts. Nevertheless, the detection of these

dark/dim H I clouds along a filament confirms what has been predicted by simulations.

4.3. Interactions in the Filament

The H I properties of filament galaxies have been characterized through a couple of recent studies. D. Kleiner et al. (2017) found that $10^9 M_\odot < M_* < 10^{11} M_\odot$ filament galaxies have H I mass fractions similar to those of control sample galaxies, galaxies at distances ≥ 5 Mpc from filament spines and selected in isolation. They also reported that filament galaxies with $M_* > 10^{11} M_\odot$ have significantly higher gas fractions compared to control sample galaxies, suggesting that the most massive galaxies are accreting cold gas from the intrafilament medium. G. Castignani et al. (2022) found an increase in H I mass and a decrease in H I deficiency with increasing distance from the filament spine for filament galaxies with $M_* \gtrsim 10^9 M_\odot$. They suggested that the observed H I deficiency is due to tidal interactions or ram pressure stripping since the deficient systems were preferentially found in dense regions within filaments.

The H I mass measurements for three of the galaxies in the narrow filament (presented in Table 2) show that two of them (G3 and G4) are quite rich in their gas content (with H I masses above average for their stellar masses; see B. Catinella et al. 2018 for the $M_* - M_{\text{H I}}$ relation of nearby galaxies). But we do find signatures of interaction and mergers for these galaxies. A detailed study of the unusually disturbed H I in G3 is presented in M. Arabsalmani et al. (2022), revealing a uniquely unusual morphology and kinematics of H I in this otherwise apparently normal galaxy. This study explored several scenarios to explain the unusual H I structure and concluded that the most viable explanation was the penetrating passage of a satellite through the disk only a few Myr ago, redistributing the H I in the galaxy without yet affecting its stellar distribution. The study mentioned how such disturbed gas could play an important role in the formation of massive stars like the progenitor of GRB 171205A. We also find the distribution of H I in G4 disturbed and detect a tail for the H I disk of G5. A detailed study of the perturbed/unusual systems in the filament will be presented in an upcoming study (M. Arabsalmani et al. 2025, in preparation).

E. Tempel et al. (2015) studied the alignment between satellites and surrounding large-scale structure using the Sloan Digital Sky Survey and found a significant alignment between satellite galaxy position and filament axis. Similar results were found in the Millennium simulations (see E. Tempel et al. 2015, and references therein). The disturbed distribution of gas in the star-forming galaxies in the filament is therefore likely to be due to interaction with gas-rich systems in the filament. Such systems are believed to aid the formation of stars in galaxies by providing them the required gas reservoirs and by potential interactions and mergers with them. This scenario is supported by the presence of the dark clouds that we have detected in the filament. Deeper H I 21 cm emission line observations are planned to explore the presence of low-mass, gas-rich systems in the vicinity of the star-forming galaxies in the filament.

5. Summary

We have identified an extremely straight and narrow filament of galaxies in the nearby Universe. The filament has a length of

5 Mpc. The eight galaxies with a spectroscopic, measured redshift on the filament are within very small distances from the filament axis, varying from 7 to 104 kpc. The redshifts of these galaxies are in a small range between $z = 0.03609$ and $z = 0.03702$, so their radial velocity with respect to their median redshift varies from ~ -210 to ~ 70 km s⁻¹, similar to the proper motions of galaxies. Most of these galaxies are actively forming stars, unlike what is expected from the statistical studies of filament galaxies in the nearby Universe, which find the majority of galaxies close to the filament spine to be passive galaxies. Their stellar masses are within a range of $10^{9.1} - 10^{10.7} M_\odot$. We search in the filament catalogs built based on TNG simulations in order to find filaments with similar geometrical and galaxy properties. We find no direct match. This, however, might be due to the methods used in building up the simulated catalogs, which likely introduce certain biases in the catalogs. We further use the full-sky mock galaxy catalog of the MillenniumTNG simulation project and search for galaxy distributions with similar geometrical properties. We find that fairly straight filaments can be found and are expected in the Λ CDM galaxy distribution as well. Our analysis shows that the identified filament is indeed unusual and rare but not exceptionally uncommon.

We study the distribution of cold gas in a 1.3 Mpc long section of the filament through H I 21 cm emission line observations and find about a dozen H I sources. Their H I masses vary between $\sim 10^{8.5}$ and $10^{9.5} M_\odot$, and they are all detected at H I column densities $N(\text{H I}) \gtrsim 10^{20}$ cm⁻². All of these detected H I sources have no confirmed optical counterparts in our deep CFHT observations. Their extreme $M_{\text{H I}}/M_*$ values imply that they are very dark. This, together with the large velocity widths of the H I 21 cm emission lines of the clouds, indicates that they might not yet be virialized and hence are not yet forming stars. The presence of such clouds in filaments, although predicted by simulations, had never been confirmed with observations. This is the first time that the existence of such clouds in a filament is observationally confirmed. We suspect that these clouds mark the peaks of the distribution of H I over large scales within the filament as predicted by simulations. Further observations are required to confirm this.

Acknowledgments

M.A. thanks Lister Staveley-Smith, Nirupam Roy, and Nicola Malasavi for helpful discussions. The present study is funded by the Deutsche Forschungsgemeinschaft (DFG; German Research Foundation) under Germany's Excellence Strategy—EXC-2094—390783311. S.R. acknowledges support by DFG through project No. 50082519 and the Australian Research Council Center of Excellence for All Sky Astrophysics in 3 Dimensions (ASTRO 3D) through project No. CE170100013. The National Radio Astronomy Observatory is a facility of the National Science Foundation operated under cooperative agreement by Associated Universities, Inc. This work is partly based on tools and data products produced by GAZPAR, operated by CeSAM-LAM and IAP. We are particularly grateful to Olivier Ilbert and Christophe Adami for their extensive support with GAZPAR. This research uses services or data provided by the Astro Data Lab, which is part of the Community Science and Data Center (CSDC) Program of NSF NOIRLab. NOIRLab is operated by the Association of Universities for Research in Astronomy (AURA), Inc., under a

cooperative agreement with the U.S. National Science Foundation. F.R. acknowledges support provided by the University of Strasbourg Institute for Advanced Study (USIAS) within the French national program Investment for the Future (Excellence Initiative) IdEx-Unistra.

Appendix A HI Data Reduction and Source Identification

We used the *L*-band receivers of the JVLA in the B and C configurations to map the HI 21 cm emission in the field. The observations in the B configuration were carried out on 2019 March 9, 2019 May 5, and 2022 October 16 for a total time of ~ 10.5 hr (proposal ID: VLA/2018-07-058; PI: Arabsalmani). The C-configuration observations were carried out on 2022 October 23 and 2022 October 28 for a total time of ~ 17.5 hr (proposal ID: VLA/2022-00-109; PI: Arabsalmani). “Classic” AIPS was used for the analysis of the data (E. W. Greisen 2003). For each day's data, after initial data editing and flux and bandpass calibration, a “channel-0” visibility data set was created by averaging together line-free channels. A standard self-calibration, imaging, and data-editing loop was applied on the channel-0 data set until no further improvement was seen in the continuum image on further self-calibration. At the end of the loop, the final antenna-based gains were applied to all the visibilities of the original multichannel data set. The radio continuum image made using the line-free channels at the end of the self-calibration cycle was used to subtract the continuum from the calibrated visibilities using the task UVSUB, following which the task UVLIN was also run. At this point, cumulative visibility data sets were created separately for the B and C configurations by combining the residual visibilities from the daily observations (2 and 3 days, respectively). We also combined the residual visibilities from the full 5 days in order to create a combined B+C-configuration data set.

The three sets of combined visibilities (B configuration, C configuration, and B+C configuration) were Fourier transformed to produce spectral cubes using the task IMAGR. For each configuration, we created two data cubes with optimized velocity resolutions of ~ 34 km s $^{-1}$ and ~ 50 km s $^{-1}$ to improve the statistical significance of the detected HI 21 cm emission in independent velocity channels while still having sufficient velocity resolution to accurately trace the velocity field of any detected source. In order to optimize between the SNR of the detections and the spatial resolution, robust factors of 0.5, -0.5 , and 0.5 were used for the B-configuration, C-configuration, and B+C-configuration visibilities, respectively, to create the cubes. The properties of the cubes produced are provided in Table 3. We also applied the primary beam correction using the task PBCOR. The field of view of the JVLA has a full width at half-power of $\sim 30'$ at the frequency of our observations in the *L* band. We restrict ourselves to within the HPBW, where it has a relatively flat response, in order to only detect HI emission with high sensitivity.

We identified the HI sources in the field observed following a two-step process, described below.

(i) We identified the possible HI source candidates in the field using the SoFiA software, designed for finding HI sources from 3D cubes (P. Serra et al. 2015; T. Westmeier et al. 2021).

SoFiA uses a Smooth+Clip finder, where it creates multiple HI cubes out of the original cube by smoothing it and clips pixels below a certain absolute flux level in the (original and) smoothed cubes, which are then merged over a preset merging length along the spatial and spectral dimensions to create a mask, which is then applied to the original cube to get the source fluxes out. Other than the native spatial and spectral resolution cube, we instructed SoFiA to also spatially smooth the data with Gaussian filters that are one and two synthesized beams in size and spectrally smooth the data with boxcar filters that are three and five channels in size. The absolute clip flux density was set to 4 times the (smoothed) rms noise level, with local noise normalization enabled given the varying noise across the field due to primary beam correction applied on the input cube. For the pixels thus selected, we conservatively set the minimum merging lengths to be 1 pixel only along both spatial and spectral dimensions. Finally, the reliability parameter, which filters out potential real detections based on the density of positive and negative sources in a certain parameter space (please see references above for details), was also conservatively set to a high value of 0.8, and the threshold of constant integrated SNR in the search space was set to 5.

(ii) Next, for each of the sources identified by SoFiA, we created two spectra from the 35 and 50 km s $^{-1}$ cubes using the task VIEWER of the Common Astronomy Software Applications package. The spectra were extracted from the cubes in the regions defined based on the moment zero maps created by SoFiA. Only for one source (G5), which was not identified by SoFiA, do we use the moment maps created in AIPS. This is one of the star-forming galaxies in the field located very close to the edge of the HPBW of JVLA. We apply the task MOMNT to the spectral cube in order to obtain maps of the HI total intensity and the intensity-weighted velocity field for this source. MOMNT works by masking out pixels in the spectral data cube that lie below a threshold flux in a secondary data cube created by smoothing the original cube both spatially and along the velocity axis—the smoothing ensures that any localized noise peaks are ignored, and only emission correlated spatially and in velocity is chosen. We created the secondary data cube by applying Hanning smoothing across blocks of three consecutive velocity channels, whereas, spatially, a Gaussian kernel of FWHM equal to 12 pixels (about twice the size of the synthesized beam) was applied. The threshold flux used to select pixels was approximately 1.5 times the noise in a line-free channel of the original cube.

Finally, we only keep those detected HI sources that have SNRs of 5 and above in both the 35 and 50 km s $^{-1}$ cubes. We measured the HI integrated flux density by integrating over the adjacent channels with fluxes above the rms noise and converted this to a HI mass (M. Meyer et al. 2017). We also fitted a Gaussian function to the HI 21 cm emission line to measure the redshift and the FWHM of the emission. Our final list of detected HI sources is provided in Table 2. The total intensity maps and the intensity-weighted velocity maps of the HI 21 cm emission line for the detected HI sources are presented in Figure 5. The extracted HI 21 cm emission spectra are shown in Figures 6 and 7.

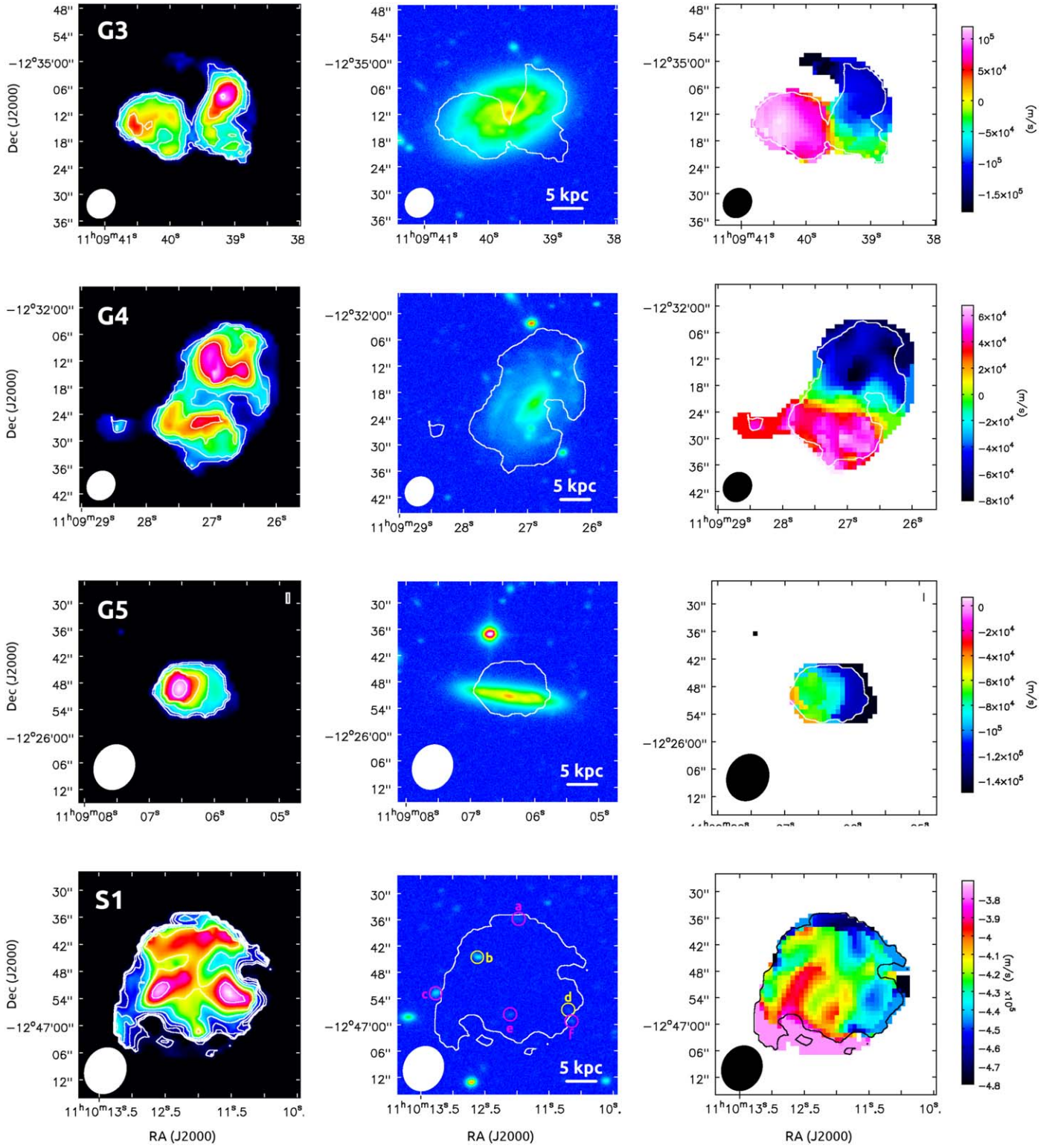


Figure 5. Each row presents a source listed in Table 2. Left: Total intensity map of H I 21 cm emission line in color, overlaid with contours of H I 21 cm emission line. The outermost contour marks the 3σ level of emission in a single channel with a velocity width of 34 km s^{-1} (equivalent to the H I column densities provided in Table 2). Each subsequent contour is in multiples of $\sqrt{2}$. Middle: The r -band CFHT image, overlaid with the 3σ contour of H I 21 cm emission line. The detected optical sources are marked with their identification numbers and circles. For sources marked with red color, association with the filament is ruled out based on photometric redshift measurements. For the sources marked with yellow color (listed in Table 5), $z = 0.037$ is not ruled out. Right: The intensity-weighted velocity map of H I 21 cm emission line in color, overlaid with the 3σ contour of H I 21 cm emission line. The size of the images in all panels are $50'' \times 50''$ except for S12 where the image sizes are $100'' \times 100''$. The synthesized beam of JVLA observations is shown in the bottom left corners of the maps.

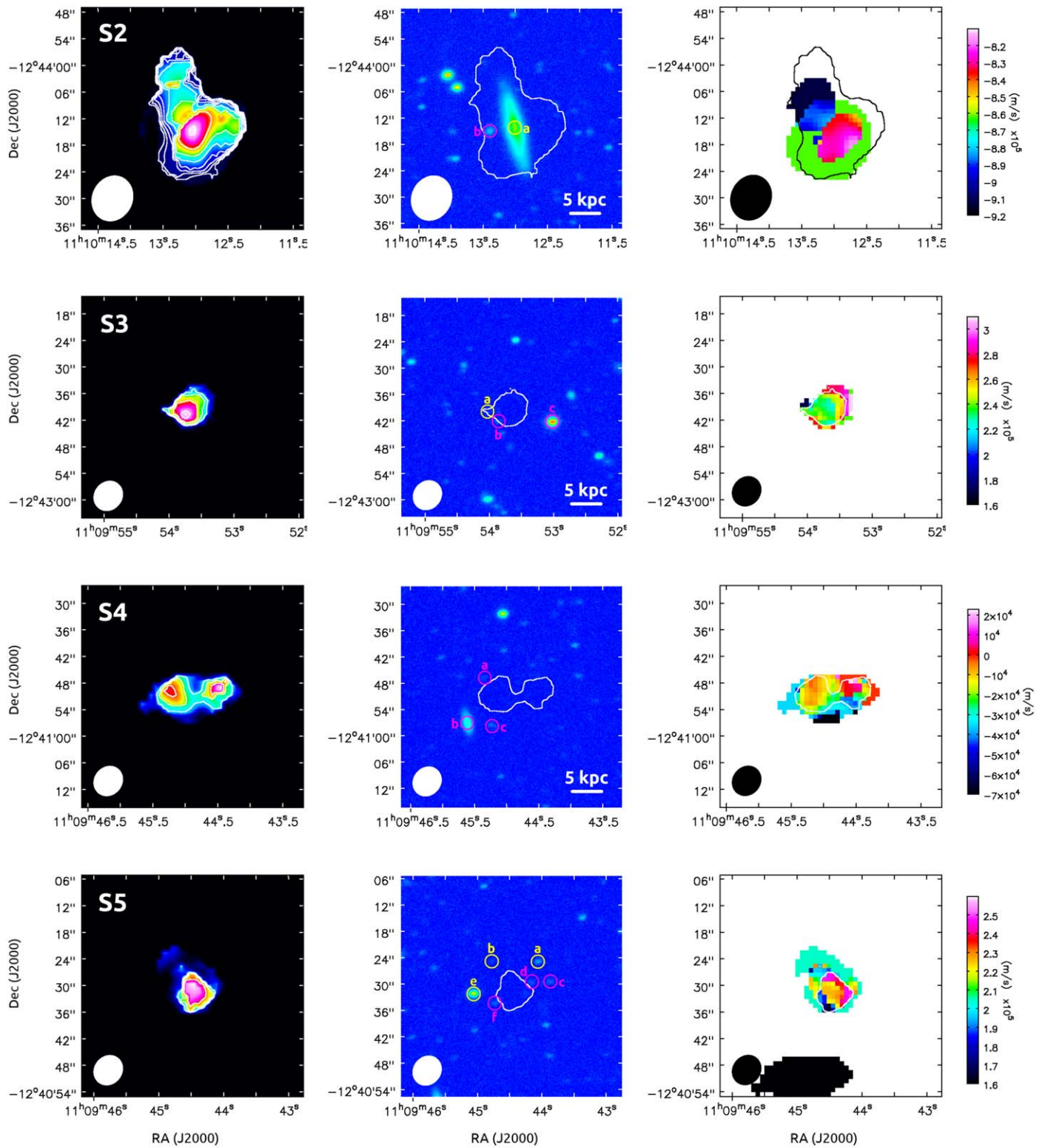


Figure 5. (Continued.)

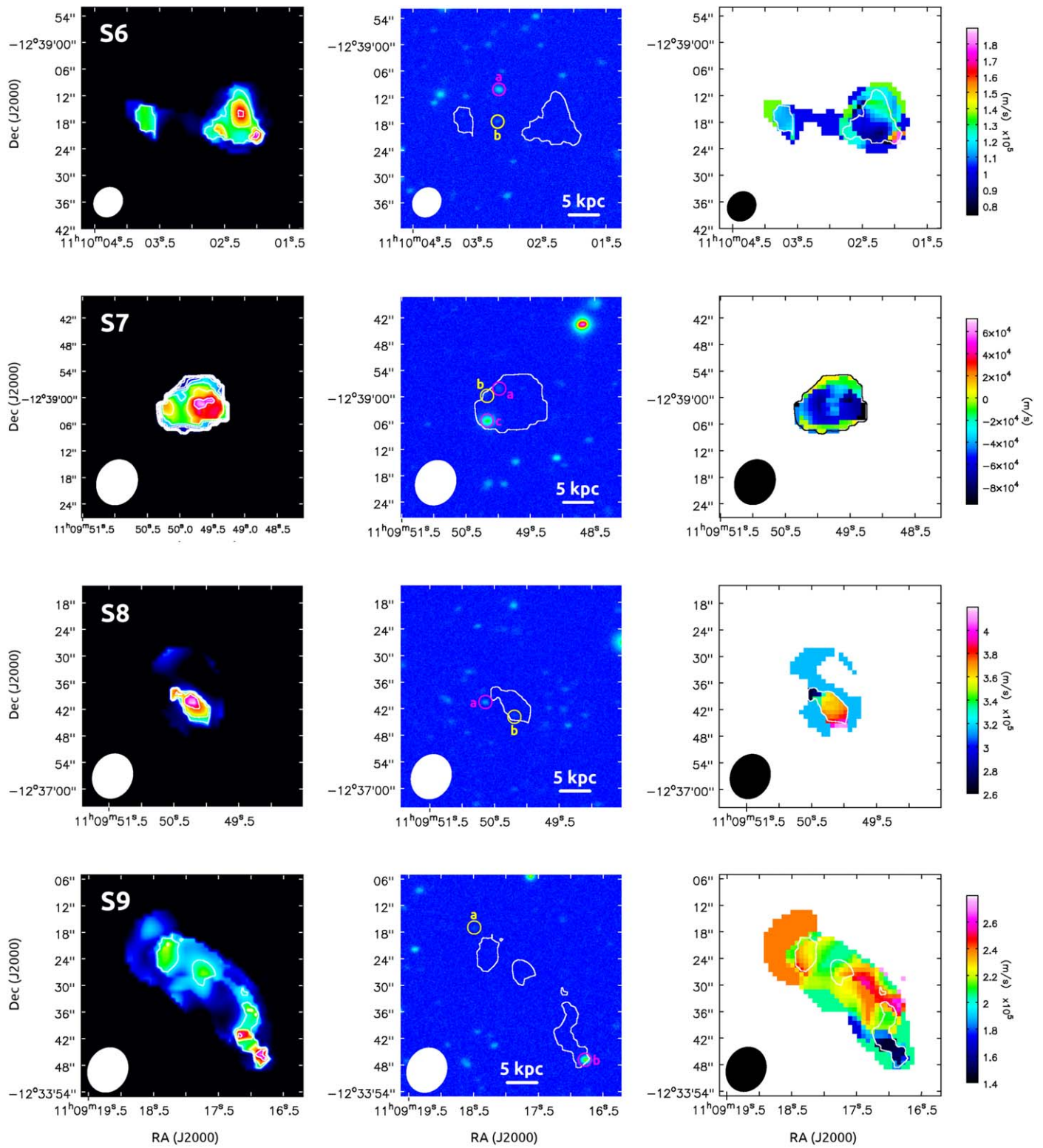


Figure 5. (Continued.)

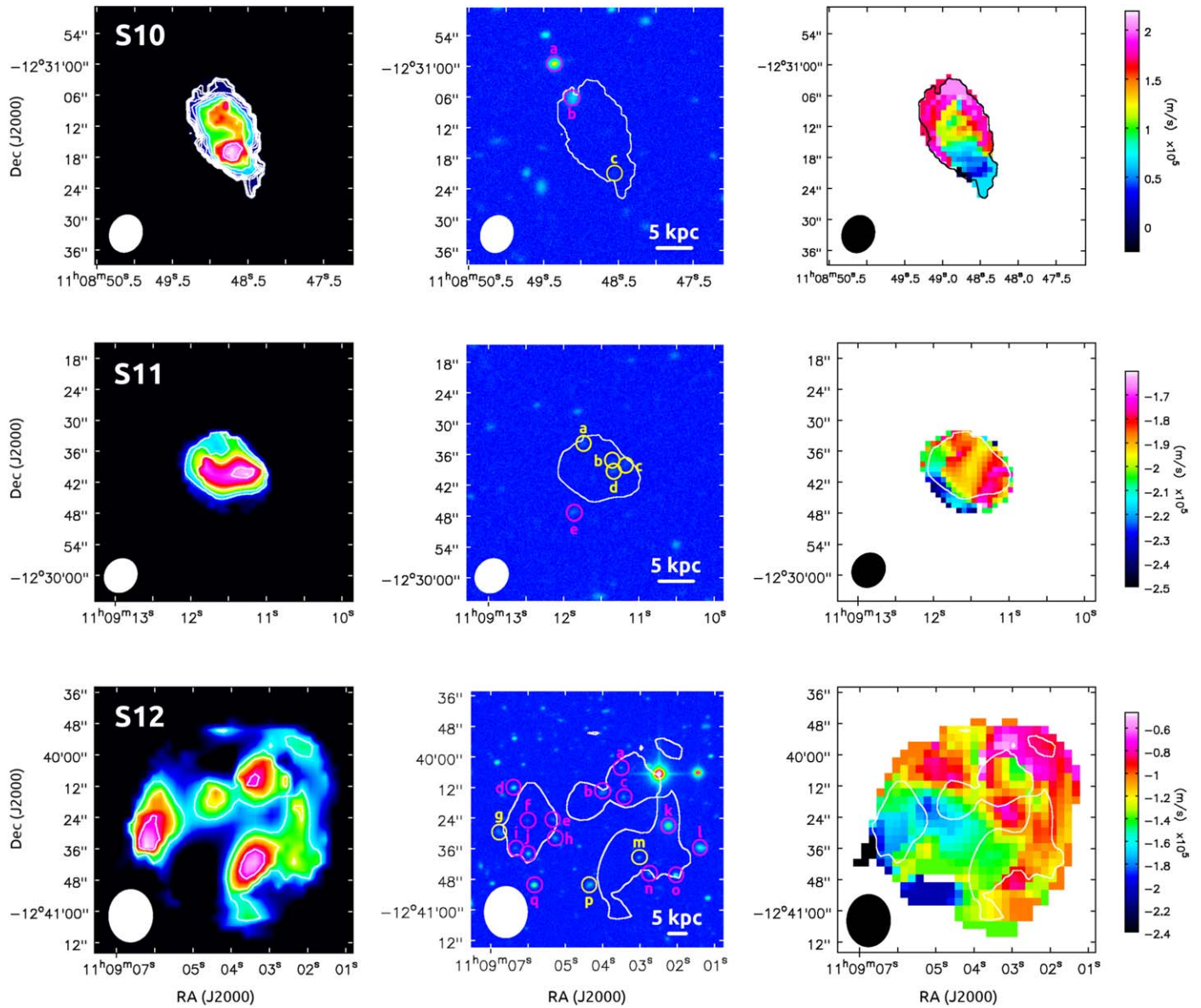


Figure 5. (Continued.)

Table 3
Parameters of the JVLA H I Data Cubes

Array	Synthesized Beam (arcsec × arcsec)	Channel Width (km s ⁻¹)	Noise in Line-free Channel (mJy beam ⁻¹)
B	7.5 × 6.4	34.2	0.20
B	7.5 × 6.4	51.3	0.17
B+C	10.5 × 9.1	34.2	0.14
B+C	10.5 × 9.1	51.3	0.11
C	20.3 × 17.0	34.2	0.18
C	20.3 × 17.0	51.3	0.15

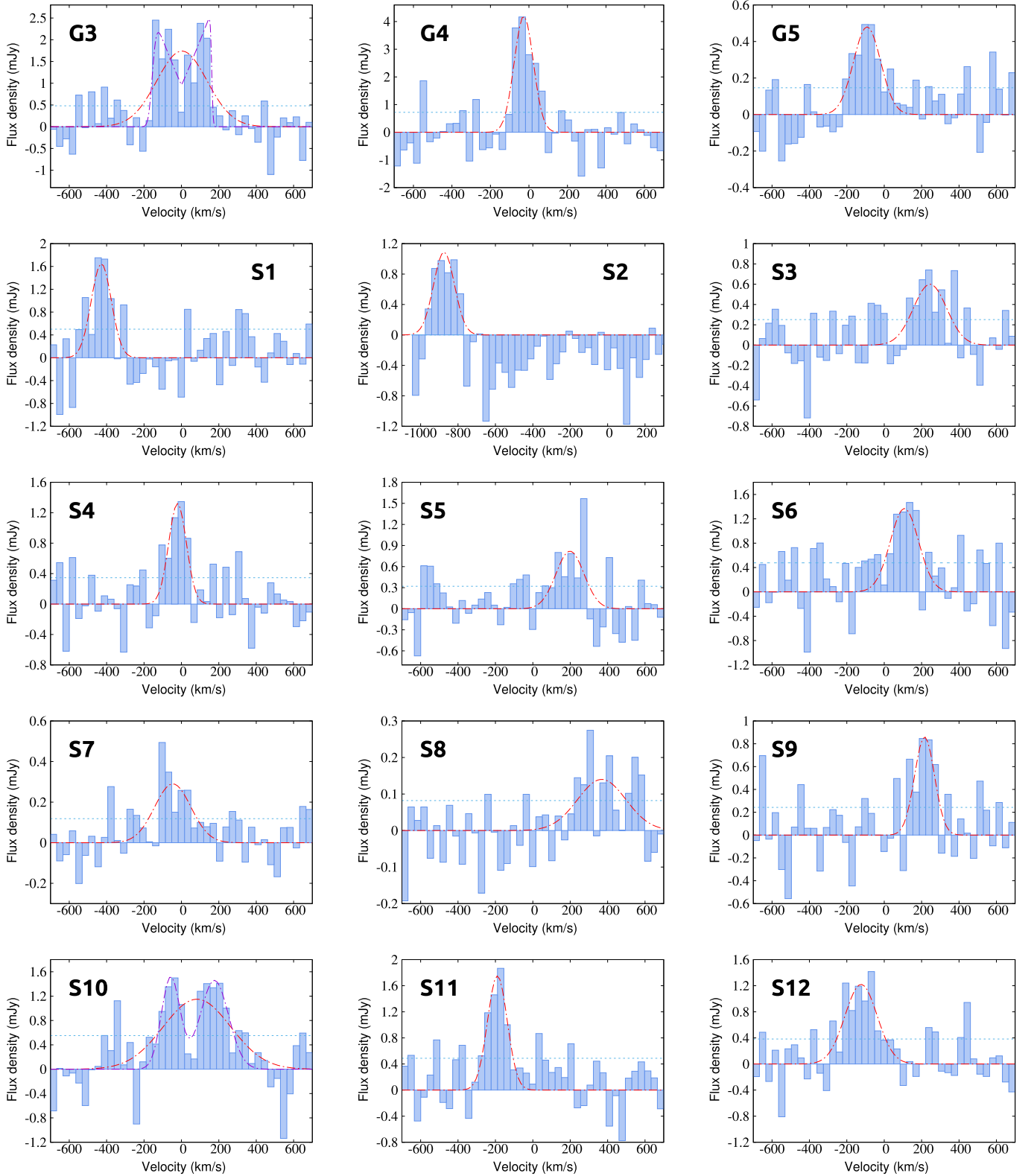


Figure 6. H I 21 cm emission spectra of detected H I sources listed in Table 2. All the spectra are extracted from the cube with 35 km s^{-1} channels (see Table 3). The blue-dotted line marks the rms noise level. The best-fitted Gaussian functions to the spectra are shown with red-dotted-dashed lines. For G3 with a double-horn-like H I spectrum, we also fitted a busy-function (T. Westmeier et al. 2014) to the H I 21 cm emission line, presented by the purple-dotted-dashed line. This results to a $\Delta v_{0.037}$ of -5 km s^{-1} , and an FWHM_{HI} of 317 km s^{-1} , consistent with those obtained by fitting a Gaussian. The H I 21 cm emission line from S10 seemed to be like a double-horn emission line; but after carefully checking the H I 21 cm emission in individual channels, we concluded the emission to originate from at least two individual components. We therefore fitted a double-Gaussian function to the H I spectrum of this source to have a better understanding of its velocity spread. This is presented with the purple-dotted-dashed line.

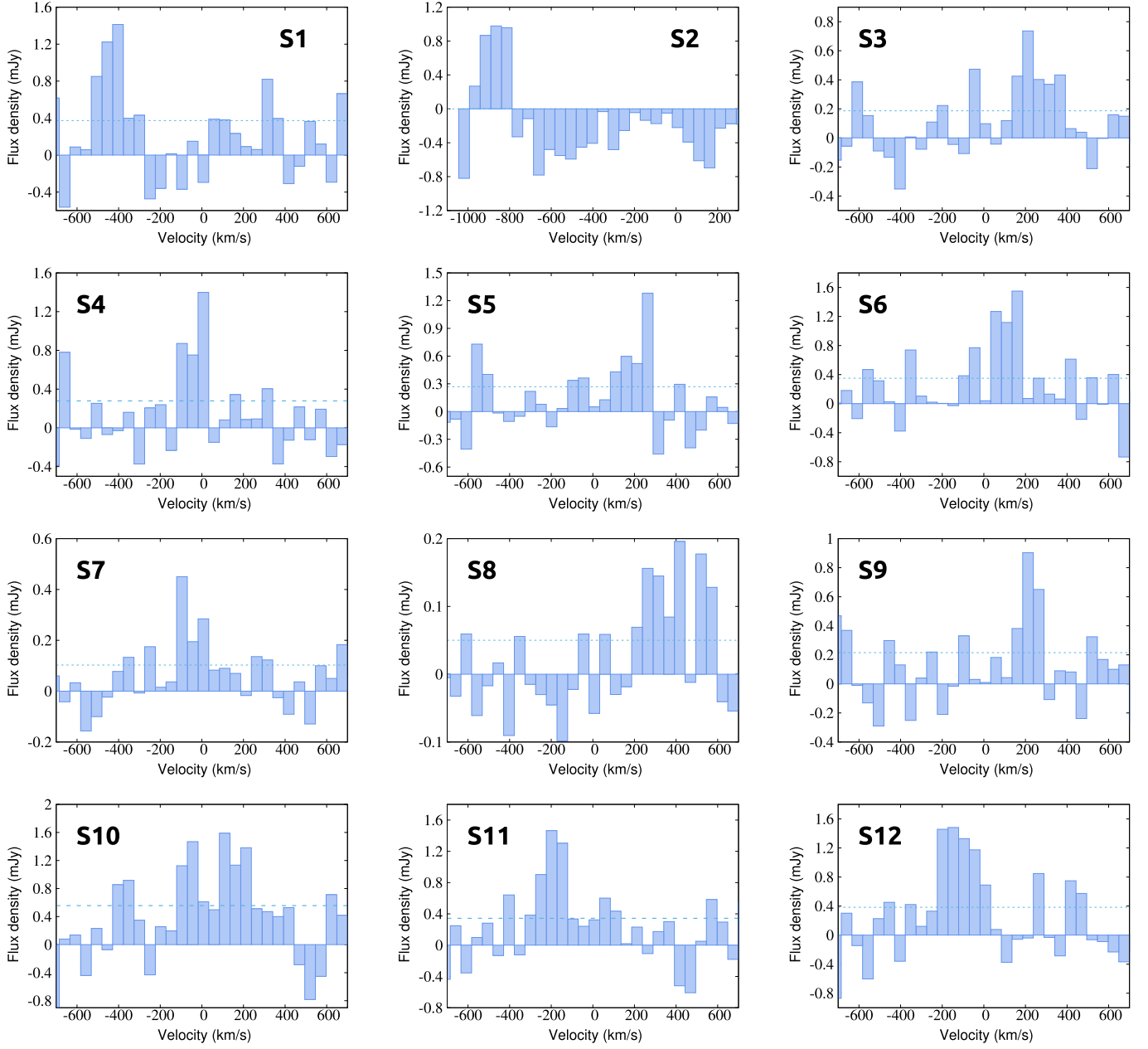


Figure 7. H I 21 cm emission spectra of S1–S12 listed in Table 2, extracted from the cube with 50 km s^{-1} channels (see Table 3), for comparison with the spectra presented in Figure 6. The blue-dotted line marks the rms noise level.

Appendix B SED Modelings

The optical magnitudes of the eight galaxies (G1–G8) are provided in Table 4, and the SED models of them are presented

in Figure 8. For the optical counterpart candidates with $\gtrsim 1\%$ probability of having $z_{\text{phot}} \lesssim 0.1$, the derived properties are listed in Table 5.

Table 4
The Optical AB Magnitudes of the Eight Galaxies That Reside along a Narrow Filament Shown in the Right Panel of Figure 1

ID	GALEX-FUV	GALEX-NUV	Pan-STARRS- <i>g</i>	Pan-STARRS- <i>r</i>	Pan-STARRS- <i>i</i>	Pan-STARRS- <i>z</i>
G1
G2	...	21.08 ± 0.17	15.767 ± 0.00154	14.9462 ± 0.00076	14.55 ± 0.00068	14.3274 ± 0.00096
G3	18.76 ± 0.12	18.19 ± 0.03	15.9313 ± 0.00228	15.3308 ± 0.00138	15.0497 ± 0.00141	14.8951 ± 0.00224
G4	19.61 ± 0.18	19.07 ± 0.05
G5	20.94 ± 0.33	20.04 ± 0.10	17.0395 ± 0.01315	16.5134 ± 0.00333	16.2298 ± 0.00291	16.0221 ± 0.00459
G6	19.43 ± 0.15	18.45 ± 0.04	15.6338 ± 0.00145	14.9911 ± 0.00103	14.6652 ± 0.00081	14.4563 ± 0.00174
G7	19.70 ± 0.17	18.78 ± 0.05	16.2019 ± 0.00394	15.6776 ± 0.00145	15.242 ± 0.00150	15.0405 ± 0.00179
G8	21.06 ± 0.35	19.34 ± 0.07	15.4931 ± 0.00087	14.9373 ± 0.00071	14.6468 ± 0.00059	14.4661 ± 0.00090
ID	Pan-STARRS- <i>y</i>	2MASS- <i>J</i>	2MASS- <i>H</i>	2MASS- <i>K_s</i>	ALLWISE-1	ALLWISE2
G1	...	16.70 ± 0.08	16.56 ± 0.10	16.61 ± 0.11	17.0 ± 0.038	17.616 ± 0.05
G2	14.0895 ± 0.00205	13.773 ± 0.044	13.468 ± 0.058	13.688 ± 0.082	14.694 ± 0.023	15.409 ± 0.024
G3	14.6917 ± 0.00500	14.515 ± 0.096	14.348 ± 0.127	14.181 ± 0.142	16.016 ± 0.026	16.51 ± 0.029
G4	18.498 ± 0.053	19.048 ± 0.128
G5	15.7913 ± 0.01054	16.762 ± 0.032	17.229 ± 0.045
G6	14.2541 ± 0.00254	13.873 ± 0.039	13.701 ± 0.052	13.896 ± 0.080	14.743 ± 0.022	15.302 ± 0.022
G7	14.8082 ± 0.00375	14.615 ± 0.069	14.393 ± 0.089	14.265 ± 0.100	15.311 ± 0.023	15.884 ± 0.025
G8	14.2366 ± 0.00162	14.028 ± 0.052	13.76 ± 0.050	13.847 ± 0.078	15.075 ± 0.033	15.671 ± 0.035
ID	MegaCam- <i>u</i>	MegaCam- <i>g</i>	MegaCam- <i>r</i>	MegaCam- <i>i</i>		
G3	16.8593 ± 0.001	15.8529 ± 0.0004	15.2587 ± 0.0004	14.9554 ± 0.0006		
G4	18.3428 ± 0.0027	17.4997 ± 0.0014	17.1106 ± 0.0014	16.955 ± 0.0029		
G5	18.2766 ± 0.0019	17.1194 ± 0.0008	16.3876 ± 0.0006	16.0618 ± 0.001		

Note. Far-UV (FUV). Near-UV (NUV). The CFHT/MegaCam magnitudes are derived as explained in Section 2.2. The urls for obtaining the other magnitudes are listed below. GALEX: <https://galex.stsci.edu/GR6/?page=mastform>. Pan-STARRS: <https://outerspace.stsci.edu/display/PANSTARRS/>. 2MASS: <https://irsa.ipac.caltech.edu/cgi-bin/Gator/nph-scan?submit=Select&projshort=2MASS>. ALLWISE: <https://irsa.ipac.caltech.edu/cgi-bin/Gator/nph-scan?submit=Select&projshort=WISE>.

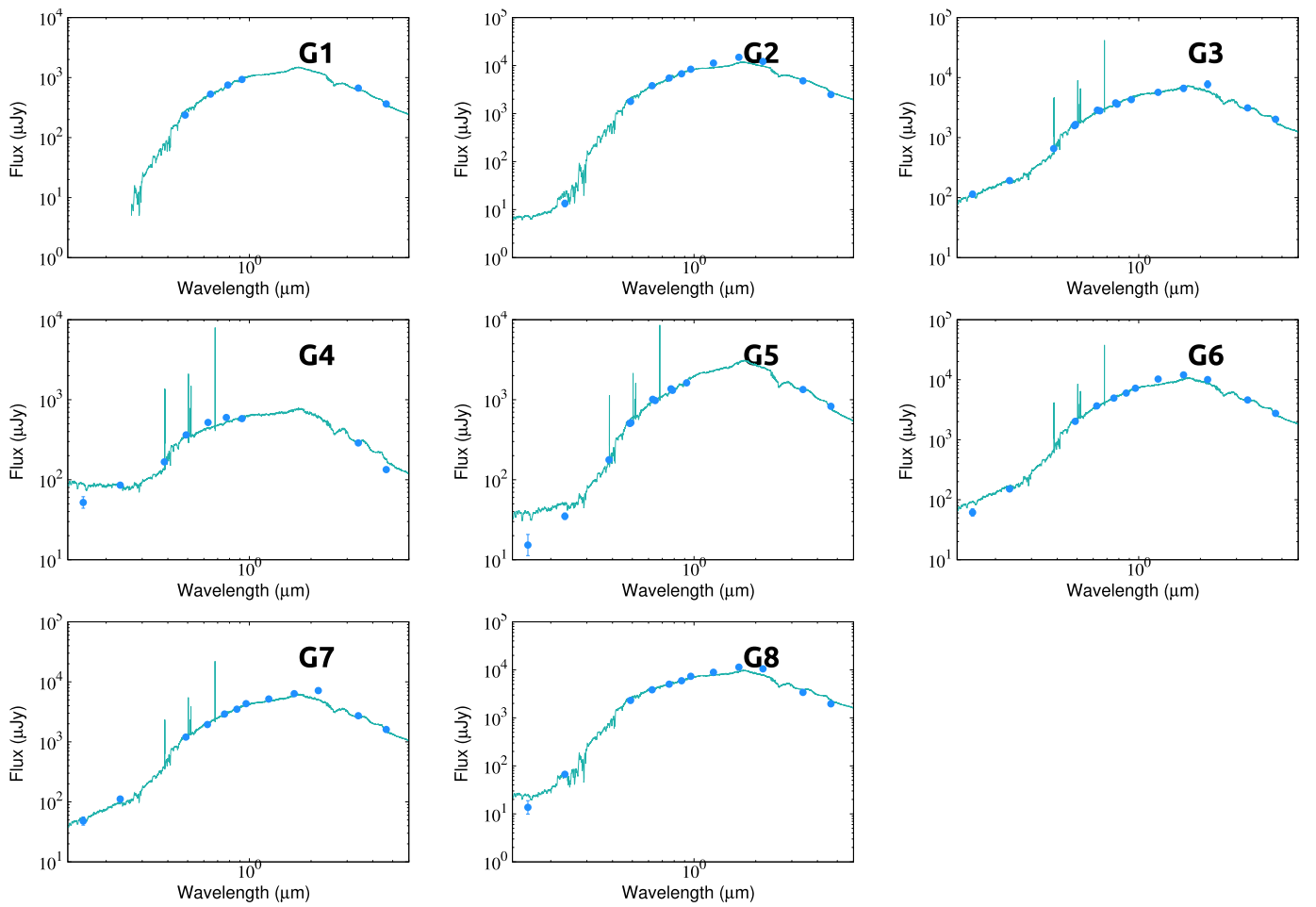


Figure 8. The fitted SED for the eight galaxies along the filament (G1–G8). The SEDs clearly demonstrate that G3–G7 are actively star-forming galaxies while G1, G2, and G8 (the three galaxies at the two ends of the filament) seem to be passive galaxies (with no emission lines). The physical properties of all galaxies, obtained from the best-fitted SEDs, are listed in Table 1.










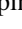


Table 5
The Properties of the Possible Optical Counterparts of the Detected H I Sources, Marked with Yellow Circles in the Middle Panels of Figure 5

H I-ID	Opt-ID	$P(z_{\text{photo}} \leq 0.1)$ %	$\log_{10}(M_*/M_{\odot})$	$\log_{10}(\text{SFR}/M_{\odot} \text{ yr}^{-1})$	$E(B - V)$	$(M_{\text{HI}}/M_*)_{\text{LL}}$
S1	b	42	7.1 ± 0.1	-7.5 ± 0.6	0	89
	d	1	6.2 ± 0.4	-2.8 ± 0.6	0.7	
S2	a	65	9.10 ± 0.03	-1.3 ± 0.1	0	1
S3	a	6	5.4 ± 0.2	-3.3 ± 0.3	0	2570
S4						10,000
S5	a	1	6.3 ± 0.1	-1.5 ± 0.2	0.7	13/5370 ^a
	b	3	5.2 ± 0.3	-3.2 ± 0.3	0	
	e	100	7.8 ± 0.1	-2.0 ± 0.1	0	
S6	b	7	6.1 ± 0.2	-2.9 ± 0.4	0	1000
S7	b	6	6.0 ± 0.3	-2.8 ± 0.5	0.3	316
S8	b	3	5.5 ± 0.3	-2.9 ± 0.4	0.4	912
S9	a	1	6.5 ± 0.3	-2.7 ± 0.4	0.5	224
S10	c	1	5.2 ± 0.3	-3.0 ± 0.3	0.2	15,488
S11	a	5	5.7 ± 0.2	-2.6 ± 0.4	0.3	96
	b	5	6.7 ± 0.3	-2.6 ± 0.7	0.7	
	c	4	6.4 ± 0.3	-2.5 ± 0.6	0.6	
	d	3	6.7 ± 0.3	-2.6 ± 0.7	0	
S12	g (93)	100	6.2 ± 0.2	-1.7 ± 0.2	0.6	28
	m (106)	11	7.4 ± 0.1	-5.4 ± 1.0	0.0	
	p (119)	49	7.3 ± 0.1	-1.4 ± 0.2	0.5	

Notes. For the listed optical sources below, the probability of having a photometric redshift $z_{\text{photo}} \leq 0.1$ obtained from SED fitting is $\geq 1\%$. Hence, we do not rule $z = 0.037$ out for these sources. The first and second columns are, respectively, the identification names and numbers of the H I sources and their possible optical counterparts. The third column is the probability of a photometric redshift $z_{\text{photo}} \leq 0.1$ for the optical source, obtained from SED fitting. Columns (4)–(6) are, respectively, stellar mass, SFR, and $E(B - V)$ obtained from SED fitting with assuming $z = 0.037$. Column (7) is the lower limit on M_{HI}/M_* , assuming that all the optical sources listed in the table could be associated with the H I sources.

^a For this source, we have provided the M_{HI}/M_* while including/excluding the optical source that is outside the H I emission (marked by “e” in Figure 5).

ORCID iDs

M. Arabsalmani  <https://orcid.org/0000-0001-7680-509X>
S. Roychowdhury  <https://orcid.org/0000-0002-5820-4589>
V. Springel  <https://orcid.org/0000-0001-5976-4599>
F. Bournaud  <https://orcid.org/0000-0002-5743-0250>
A. Burkert  <https://orcid.org/0000-0001-6879-9822>
J.-C. Cuillandre  <https://orcid.org/0000-0002-3263-8645>
P.-A. Duc  <https://orcid.org/0000-0003-3343-6284>
E. Emsellem  <https://orcid.org/0000-0002-6155-7166>
D. Galárraga-Espinosa  <https://orcid.org/0000-0002-8808-803X>
E. Pian  <https://orcid.org/0000-0001-8646-4858>
F. Renaud  <https://orcid.org/0000-0001-5073-2267>
M. A. Zwaan  <https://orcid.org/0000-0003-0101-1804>

References

- Alpaslan, M., Grootes, M., Marcum, P. M., et al. 2016, *MNRAS*, **457**, 2287
Alvarez, G. E., Randall, S. W., Bourdin, H., Jones, C., & Holley-Bockelmann, K. 2018, *ApJ*, **858**, 44
Arabsalmani, M., Roychowdhury, S., Renaud, F., et al. 2022, *AJ*, **164**, 69
Aragón-Calvo, M. A., van de Weygaert, R., & Jones, B. J. T. 2010, *MNRAS*, **408**, 2163
Arnouts, S., Cristiani, S., Moscardini, L., et al. 1999, *MNRAS*, **310**, 540
Arnouts, S., Le Floch, E., Chevillard, J., et al. 2013, *A&A*, **558**, A67
Barrera, M., Springel, V., White, S. D. M., et al. 2023, *MNRAS*, **525**, 6312
Bertin, E., & Arnouts, S. 1996, *A&AS*, **117**, 393
Bilek, M., Müller, O., Vudragović, A., & Taylor, R. 2020, *A&A*, **642**, L10
Bond, J. R., Kofman, L., & Pogosyan, D. 1996, *Natur*, **380**, 603
Bonjean, V., Aghanim, N., Douspis, M., Malavasi, N., & Tanimura, H. 2020, *A&A*, **638**, A75
Bournaud, F., Combes, F., Jog, C. J., & Puerari, I. 2005, *A&A*, **438**, 507
Brinchmann, J., Charlot, S., White, S. D. M., et al. 2004, *MNRAS*, **351**, 1151
Cannon, J. M., Martinkus, C. P., Leisman, L., et al. 2015, *AJ*, **149**, 72
Cantalupo, S., Arrigoni-Battaia, F., Prochaska, J. X., Hennawi, J. F., & Madau, P. 2014, *Natur*, **506**, 63
Castignani, G., Combes, F., Jablonka, P., et al. 2022, *A&A*, **657**, A9
Catinella, B., Saintonge, A., Janowiecki, S., et al. 2018, *MNRAS*, **476**, 875
Cautun, M., van de Weygaert, R., Jones, B. J. T., & Frenk, C. S. 2014, *MNRAS*, **441**, 2923
Cen, R., & Ostriker, J. P. 2006, *ApJ*, **650**, 560
Dekel, A., Birnboim, Y., Engel, G., et al. 2009, *Natur*, **457**, 451
Dénes, H., Kilborn, V. A., & Koribalski, B. S. 2014, *MNRAS*, **444**, 667
Dey, A., Schlegel, D. J., Lang, D., et al. 2019, *AJ*, **157**, 168
Dietrich, J. P., Werner, N., Clowe, D., et al. 2012, *Natur*, **487**, 202
Donnan, C. T., Tojeiro, R., & Kraljic, K. 2022, *NatAs*, **6**, 599
Duc, P.-A., Cuillandre, J.-C., Karabal, E., et al. 2015, *MNRAS*, **446**, 120
Eckert, D., Jauzac, M., Shan, H., et al. 2015, *Natur*, **528**, 105
Fumagalli, M., Prochaska, J. X., Kasen, D., et al. 2011, *MNRAS*, **418**, 1796
Galárraga-Espinosa, D., Aghanim, N., Langer, M., Gouin, C., & Malavasi, N. 2020, *A&A*, **641**, A173
Galárraga-Espinosa, D., Aghanim, N., Langer, M., & Tanimura, H. 2021, *A&A*, **649**, A117
Gallego, S. G., Cantalupo, S., Lilly, S., et al. 2018, *MNRAS*, **475**, 3854
Greisen, E. W. 2003, in *Information Handling in Astronomy—Historical Vistas*, ed. A. Heck (Dordrecht: Kluwer), 109
Hernández-Aguayo, C., Springel, V., Pakmor, R., et al. 2023, *MNRAS*, **524**, 2556
Higuchi, Y., Oguri, M., Tanaka, M., & Sakurai, J. 2015, arXiv:1503.06373

- Ibert, O., Arnouts, S., McCracken, H. J., et al. 2006, *A&A*, 457, 841
- Janowiecki, S., Leisman, L., Józsa, G., et al. 2015, *ApJ*, 801, 96
- Jasche, J., Kitaura, F. S., Li, C., & Enßlin, T. A. 2010, *MNRAS*, 409, 355
- Jauzac, M., Jullo, E., Kneib, J.-P., et al. 2012, *MNRAS*, 426, 3369
- Jones, D. H., Read, M. A., Saunders, W., et al. 2009, *MNRAS*, 399, 683
- Jones, D. H., Saunders, W., Colless, M., et al. 2004, *MNRAS*, 355, 747
- Jones, M. G., Haynes, M. P., Giovanelli, R., & Moorman, C. 2018, *MNRAS*, 477, 2
- Jones, M. G., Janowiecki, S., Dey, S., et al. 2024, *ApJL*, 966, L15
- Józsa, G. I. G., Jarrett, T. H., Cluver, M. E., et al. 2022, *ApJ*, 926, 167
- Kanekar, N., Braun, R., & Roy, N. 2011, *ApJL*, 737, L33
- Kent, B. R. 2010, *ApJ*, 725, 2333
- Kent, B. R., Giovanelli, R., Haynes, M. P., et al. 2007, *ApJL*, 665, L15
- Kim, S., Rey, S.-C., Bureau, M., et al. 2016, *ApJ*, 833, 207
- Kleiner, D., Pimblet, K. A., Jones, D. H., Koribalski, B. S., & Serra, P. 2017, *MNRAS*, 466, 4692
- Kondo, H., Miyatake, H., Shirasaki, M., Sugiyama, N., & Nishizawa, A. J. 2020, *MNRAS*, 495, 3695
- Kraljic, K., Arnouts, S., Pichon, C., et al. 2018, *MNRAS*, 474, 547
- Kuutma, T., Tamm, A., & Tempel, E. 2017, *A&A*, 600, L6
- Laigle, C., Pichon, C., Arnouts, S., et al. 2018, *MNRAS*, 474, 5437
- Lee-Waddell, K., Spekkens, K., Cuillandre, J. C., et al. 2014, *MNRAS*, 443, 3601
- Leisman, L., Haynes, M. P., Janowiecki, S., et al. 2017, *ApJ*, 842, 133
- Leisman, L., Rhode, K. L., Ball, C., et al. 2021, *AJ*, 162, 274
- Lu, Y. S., Mandelker, N., Oh, S. P., et al. 2024, *MNRAS*, 527, 11256
- Mahajan, S., Drinkwater, M. J., Driver, S., et al. 2018, *MNRAS*, 475, 788
- Malavasi, N., Aghanim, N., Douspis, M., Tanimura, H., & Bonjean, V. 2020, *A&A*, 642, A19
- Malavasi, N., Arnouts, S., Vibert, D., et al. 2017, *MNRAS*, 465, 3817
- Martin, D. C., Matuszewski, M., Morrissey, P., et al. 2015, *Natur*, 524, 192
- Martinet, N., Clowe, D., Durret, F., et al. 2016, *A&A*, 590, A69
- Martinez, H. J., Muriel, H., & Coenda, V. 2016, *MNRAS*, 455, 127
- Martizzi, D., Vogelsberger, M., Artale, M. C., et al. 2019, *MNRAS*, 486, 3766
- Meyer, M., Robotham, A., Obreschkow, D., et al. 2017, *PASA*, 34, 52
- Popping, A., & Braun, R. 2011a, *A&A*, 533, A122
- Popping, A., & Braun, R. 2011b, *A&A*, 527, A90
- Popping, A., & Braun, R. 2011c, *A&A*, 528, A28
- Popping, A., Davé, R., Braun, R., & Oppenheimer, B. D. 2009, *A&A*, 504, 15
- Román, J., Jones, M. G., Montes, M., et al. 2021, *A&A*, 649, L14
- Santiago-Bautista, I., Caretta, C. A., Bravo-Alfaro, H., Pointecouteau, E., & Andernach, H. 2020, *A&A*, 637, A31
- Sarron, F., Adami, C., Durret, F., & Laigle, C. 2019, *A&A*, 632, A49
- Scharf, C., Donahue, M., Voit, G. M., Rosati, P., & Postman, M. 2000, *ApJL*, 528, L73
- Serra, P., Westmeier, T., Giese, N., et al. 2015, *MNRAS*, 448, 1922
- Shectman, S. A., Landy, S. D., Oemler, A., et al. 1996, *ApJ*, 470, 172
- Sorgho, A., Hess, K., Carignan, C., & Oosterloo, T. A. 2017, *MNRAS*, 464, 530
- Sousbie, T. 2011, *MNRAS*, 414, 350
- Sousbie, T., Pichon, C., Courtois, H., Colombi, S., & Novikov, D. 2008, *ApJL*, 672, L1
- Springel, V., Frenk, C. S., & White, S. D. M. 2006, *Natur*, 440, 1137
- Springel, V., White, S. D. M., Jenkins, A., et al. 2005, *Natur*, 435, 629
- Steer, I., Madore, B. F., Mazzarella, J. M., et al. 2017, *AJ*, 153, 37
- Tanimura, H., Aghanim, N., Bonjean, V., Malavasi, N., & Douspis, M. 2020a, *A&A*, 637, A41
- Tanimura, H., Aghanim, N., Kolodzig, A., Douspis, M., & Malavasi, N. 2020b, *A&A*, 643, L2
- Tanimura, H., Hinshaw, G., McCarthy, I. G., et al. 2019, *MNRAS*, 483, 223
- Tempel, E., Guo, Q., Kipper, R., & Libeskind, N. I. 2015, *MNRAS*, 450, 2727
- Tempel, E., Stoica, R. S., Martinez, V. J., et al. 2014, *MNRAS*, 438, 3465
- Umehata, H., Fumagalli, M., Smail, I., et al. 2019, *Sci*, 366, 97
- Westmeier, T., Jurek, R., Obreschkow, D., Koribalski, B. S., & Staveley-Smith, L. 2014, *MNRAS*, 438, 1176
- Westmeier, T., Kitaëff, S., Pallot, D., et al. 2021, *MNRAS*, 506, 3962
- Wong, O. I., Stevens, A. R. H., For, B. Q., et al. 2021, *MNRAS*, 507, 2905
- Zel'dovich, Y. B. 1970, *A&A*, 5, 84
- Zwaan, M. A., Meyer, M. J., Staveley-Smith, L., & Webster, R. L. 2005, *MNRAS*, 359, L30